DRAFT: March 18, 2007

The Formation and Evolution of Planetary Systems: Data Reduction Methods for IRAC, MIPS, and IRS Low-resolution Data

John M. Carpenter[1]

Jeroen Bouwman[2]

Murray D. Silverstone[3]

Jinyoung Serena Kim[3]

Dean C. Hines[4]

John Stauffer[5]

Martin Cohen[6]

Michael R. Meyer[3]

ABSTRACT

We summarize the procedures adopted by the Formation and Evolution of Planetary Systems (FEPS) *Spitzer* legacy program for the reduction of IRAC, MIPS, and IRS data. The image processing steps closely follow the general recommendations from the *Spitzer* instrument teams and the *Spitzer* science team. Photometric repeatability better than 1.2% is achieved for the IRAC data. The relative photometry between the IRAC 8μm and MIPS 24μm is 1.6% for stars brighter than 100 mJy at 24μm, and 3.6% for stars with 24μm flux densities between 1 and 100 mJy.

Subject headings:

---

[1]Department of Astronomy, California Institute of Technology, Mail Code 105-24, 1200 East California Boulevard, Pasadena, CA 91125.

[2]Max-Planck-Institut fr Astronomie, D-69117 Heidelberg, Germany.

[3]Steward Observatory, The University of Arizona, 933 North Cherry Avenue, Tucson, AZ 85721.

[4]Space Science Institute, 4750 Walnut Street, Suite 205, Boulder, CO 80301.

[5]Spitzer Science Center, California Institute of Technology, Mail Code 314-6, 1200 East California Boulevard, Pasadena, CA 91125

[6]Radio Astronomy Laboratory, University of California, Berkeley, CA 94720

1. Introduction

The Formation and Evolution of Planetary Systems (FEPS) Spitzer legacy science program is designed to trace the evolution of planetary systems around solar-type stars with ages ranging from: 1) 3-10 Myr when stellar accretion from the disk terminates; to 2) 10-100 Myr when planets achieve their final mass via coalescence of solids and accretion of remnant gas; to 3) 100-1000 Myr when the final architecture of solar systems takes form and frequent collisions between remnant planetesimals produce copious quantities of dust; and finally to 4) mature systems of age comparable to the sun in which planet-driven activity of planetesimals continues to generate detectable dust. To achieve these goals, FEPS obtained spectro-photometric observations for 328 stars spanning ages between 3 Myr and 3 Gyr as described in Meyer et al. (2006). The observing strategy is to trace the spectral energy distribution (SED) from 3.6μm to 70μm using broad-band IRAC and MIPS photometry, and to measure the SED shape between 8 and 35μm with IRS low-resolution spectra. In addition, MIPS 160μm photometry was obtained for 40 stars to search for colder dust, and high-resolution IRS spectra were obtained for 10 sources to search for molecular gas. Most observations of the FEPS source list were obtained as part of the FEPS program, although some stars were also observed in GTO or the c2d Spitzer Legacy programs (Evans et al. 2003).

Preliminary data for a subset of the FEPS sample have been previously reported by Meyer et al. (2004), Kim et al. (2005), Silverstone et al. (2006), and Hines et al. (2006). The high-resolution data reduction procedures are presented in a series of papers on the gas content of the FEPS team (Hollenbach et al. 2005; Pascucci et al. 2006, 2007) and are not repeated here. This paper summarizes the final data reduction procedures adopted by the FEPS program for the IRAC, MIPS, and IRS low-resolution spectrometer observations. The IRAC and MIPS photometry is presented in Table 1.

2. IRAC

The FEPS team obtained IRAC (Fazio et al. 2004) observations for 311 stars of the 328 in the sample. The remaining 17 objects were observed by other Spitzer programs, including 16 Hyades stars in a Guaranteed Time Observations (GTO) program led by G. Fazio, and one source (ScoPMS 214) in the Upper OB Association by the c2d Legacy Program (Evans et al. 2003).

FEPS IRAC observations were conducted in subarray mode with a four-point dither pattern and the medium dither scale. In subarray mode, each IRAC band is observed separately where a 32×32 pixel section ($39'' \times 39''$) of the 256×256 pixel full-array ($5.2' \times 5.2'$) is read out at a frame-time of 0.02, 0.10, or 0.40 seconds. At each dither position, 64 images are taken at the same frame-time for a total of 256 images per channel. The location of the four dither positions are the same for each source to within the pointing accuracy of the spacecraft. Five FEPS source were observed in all four IRAC bands for the initial verification observations (Meyer et al. 2004).

Channel 3 (5.8μm) observations were dropped for the remaining sources since it had the lowest signal-to-noise ratio (SNR) of the four IRAC channels.

IRAC GTO observations of the 16 Hyades stars and c2D observations of ScoPMS214 were observed in all four IRAC channels in full-array, high-dynamic-range mode where a 0.6 sec integration is followed by a 12 sec exposure. The Hyades stars were observed at three dither positions in his manner, and ScoPMS 214 at two positions. The long-integration times in IRAC channels 1, 2, and 3 were saturated and were not processed further.

2.1. Image Processing

Data analysis was performed on Basic Calibrated Data (BCD) products generated by the *Spitzer* Science Center (SSC) data reduction pipeline version S13. The SSC pipeline removes the electronic bias, subtracts a dark image, applies a flat field correction, and linearizes the pixel response. Additional processing on the BCD images was performed by the FEPS team as now described.

For the subarray data, cosmic ray hits were identified and flagged by filtering the sequence of 64 frames at each dither position. At a given pixel, the median and RMS of the 64 frames values were computed using the median absolute deviation. Any pixels that deviated from the mean by more than $n\sigma$ were flagged, where n was calculated to correspond to a probability of 10^{-4} that such an outlier pixel could occur by gaussian noise. The median and dispersion were recomputed in an iterative fashion until no additional pixels were flagged. For 26 frames (or 0.03% of the data), the cosmic ray hit near the source and the entire image was discarded. For sources HD 77407 and HD 70516, we removed all frames at two dither positions where the FEPS target position overlapped with a latent image.

For the archival full-array observations, cosmic-ray rejection was performed using the MOPEX (Makovoz & Marleau 2005) mosaicking package distributed by the SSC [1]. Images were aligned astrometrically and the RMS was computed using the median absolute deviation at each pixel position. Pixel values that deviated more than 5 times the RMS from the median were removed.

After outlier rejection, both the sub- and full-array images were multiplied by the photometric correction images produced by the SSC that correct for variations in the pixel area and the effective response of the filters across the IRAC focal plane[2]. These corrections images were derived by observing a star at 225 positions across the full array, and thus tie the calibration of the sub- and full-array observations. The nominal pixel scales of the IRAC data after applying the correction images are 1.221, 1.213, 1.222, and 1.220 arcseconds for channels 1, 2, 3, and 4 respectively.

[1] http://ssc.spitzer.caltech.edu/postbcd/

[2] http://ssc.spitzer.caltech.edu/irac/calib/

2.2. Photometry

IRAC photometry on the full- and sub-array images was measured using a modified version of IDLPHOT[3]. Aperture photometry was performed on each frame with an aperture radius of 3 pixels and a sky annulus centered on the source with an inner radius of 10 pixels and a width of 10 pixels. The pixel values in the sky-annulus were sigma-clipped using the median absolute deviation, and the sky value was estimated as the mean of the remaining pixels. For several sources, an accurate centroid could not be derived on individual frames, and a subset of frames were coadded until the positional uncertainty was less than 0.1 pixels. For IRAC channel 1, the measured flux depends on the position of the star in the pixel (M. Silverstone, private communication); a correction was applied to based on the measured centroids using the formalism described by Reach et al. (2005). Fluxes were then computed as the unweighted average of the individual measurements.

Aperture corrections are needed to convert the photometry to the fiducial 10-pixel aperture used to calibrate the IRAC instrument (Reach et al. 2005). The aperture corrections derived from the FEPS data for a 3-pixel wide aperture are 1.109, 1.110, 1.107, and 1.200 for IRAC channels 1, 2, 3, and 4 respectively. These aperture corrections agree with the values listed on the SSC website to within 0.4% for channels 1 and 2, and 1.6% for channels 3 and 4. The aperture correction measured for 23 sources deviated by more than 3σ from the sigma-clipped mean of all stars. Twenty of these sources are known from an adaptive optic survey to be multiple systems with $\sim 2''$ separation between the primary and secondary stars (Metchev & Hillenbrand 2006). The other three sources have not been observed at high resolution and the multiplicity status is unknown. The aperture correction at a four pixel radius derived in a similar manner for these 23 sources is within 1.3% of the nominal correction for each source, and therefore a four pixel aperture radius and an aperture correction of 1.069, 1.079, 1.066, and 1.081 was used for IRAC channels 1, 2, 3, 4 respectively.

Internal photometric uncertainties were computed as $\sigma_{\rm RMS}/\sqrt{n}$, where $\sigma_{\rm RMS}$ is the standard deviation of the n individual dither positions for the subarray observations or individual frames for full-array. The RMS of the flux, normalized by the mean flux, measured at the four sub-array dither positions is plotted versus the mean flux in Figure 1. For channels 1 and 2, the normalized RMS shows no trend with the mean flux, while for channel 4, the normalized RMS increases systematically toward the fainter fluxes for a fixed frame time as expected if the repeatability is photon-limited. The repeatability of the photometry measured for the 64 frames at a fixed dither position indicates that the photometric repeatability between the four dither positions should be less than 0.4% (1σ) in each channel for the brighter stars. Given that the repeatability between dithers is larger than these limits, the precision of the photometry is limited by either our data reduction procedures or instrument limitations in obtaining dithered data. Therefore, for channels 1 and 2, we adopt a minimum internal uncertainty of 0.72% and 1.22% respectively, which corresponds to the median repeatability from the ensemble data shown in Figure 1. For channel 4, we adopt a minimum

[3]http://idlastro.gsfc.nasa.gov

uncertainty of 0.66%, which was computed as the median value for stars with a repeatability less than 1.2%.

The IRAC photometry and internal uncertainties are presented in Table 1. The flux measurements are tied to the calibration described in Reach et al. (2005) with calibration factors of 0.0188, 0.1388, and 0.2021 MJy/sr per DN/s for IRAC 3.6, 4.5, 4.5, and 8μm respectively. The estimated calibration uncertainty is 2% in each band.

3. MIPS 24μm

The FEPS team obtained MIPS 24μm (Rieke et al. 2004) observations for 323 sources, and data were extracted from the *Spitzer* archive for five objects. The exposure time was 3 or 10 sec depending on the estimated photospheric brightness of the star, and 28 or 56 dithered images were obtained for each star to achieve a signal to noise of at least 30 on the stellar photosphere.

3.1. Image Processing

MIPS 24μm images were processed with SSC pipeline version S13. Individual BCD images containing the "strong" jailbar effect caused by bright sources or cosmic rays were removed. Individual images were also removed that had anomalous fluxes caused by cosmic ray hits near the expected source position. These images were identified by performing aperture photometry on individual BCD images for a given source, and identifying outlier fluxes or centroid coordinates from the mean that had less than a 10^{-4} chance to have been caused by random noise.

Once contaminated BCD images were removed, additional processing steps were performed following the recommendations from the SSC MIPS handbook and the MIPS instrument team (Engelbracht et al. 2006). Image background levels for a each source were first adjusted to a common median value by an additive constant on a frame-by-frame basis to compensate for time-variable background levels. Images for each source were then median combined to derive a flat-field correction that removed long term gain changes. During the median filtering, a 5-pixel radius region centered on the source position was masked, and a 3σ clipping algorithm was used to remove outliers. The resulting median image was normalized to unity by dividing by the median pixel value across the image. Flat field images were derived only for sources that did not have spatially variable nebulosity that would contaminate the flat field images. Affected sources were identified from visual inspection of the image mosaics. If nebulosity is present in the mosaic, a flat-field image from another FEPS source was used that was a) obtained within a time interval $\pm$ 1 day, b) had the same exposure time, and c) had the closest matched background level. If no such image existed, the image nearest in time with the same exposure time was used.

3.2. Photometry

Photometry was performed using the MOPEX package (Makovoz & Marleau 2005). First, the BCD images for a given sources were stacked according to position on the sky using the World Coordinate System (WCS) in the image headers, and cosmic ray rejection was performed by removing pixels within the stack that deviated by more than 5σ from the mean. Point sources were identified on a mosaic of the BCD images using a 10σ detection threshold. The resulting detection lists were examined and edited as necessary to remove apparently false sources and to add any sources missed by the automated detection method.

Point-spread-function (PSF) fitting photometry was performed using the APEX module in MOPEX. The empirical PSF distributed with the APEX package was fitted to the individual BCD images simultaneously (as opposed to the mosaicked image) using a fitting area of 21×21 pixels for most images. A 5×5 pixel fitting area was used for eight sources that have spatially variable nebulosity near the point source position. From visual inspection of the mosaicked images, other 24μm sources often overlapped with the FEPS target and were fitted with a PSF simultaneously. The free parameter include a spatially-constant sky background level, the peak fluxes for each source in the fit, and the centroid positions.

Photometry was measured by integrating the PSF to a radius of 3 pixels (1 pixel $\sim 2.55''$). An aperture correction is then needed to place the PSF photometry on the same zero-point scale as that adopted by the MIPS team. First, aperture photometry was performed on the individual BCD images using a customize version of IDLPHOT with an aperture radius of $13''$ and a sky annulus between $20''$ and $32''$. These aperture parameters correspond to a set that have been previously calibrated by the MIPS instrument team. Photometry was performed on the individual BCD images, and the results averaged. The average ratio of the flux measured with aperture photometry compared to PSF photometry is 1.371 with a RMS of 0.011 for 108 sources brighter than 20 mJy. From the SSC web pages, the aperture correction for the adopted aperture radius and sky annulus is a 1.167. Therefore, the PSF fluxes were multiplied by the produce of these factors, 1.600, to obtain the final fluxes.

APEX computes the internal photometric uncertainties based on the signal to noise of the source in the image. For many sources the computed uncertainty was much smaller ($<<$ 1%) than can be achieved based on repeated observations of the source. The minimum internal uncertainty was therefore estimated based on photometric repeatability from aperture photometry. The normalized RMS of the MIPS 24μm fluxes measured from *aperture* photometry on individual BCD images is presented in Figure 2. The variation in the RMS is higher for fainter sources for a given exposure time as expected if the uncertainties are photon-limited. For sources brighter than 100 mJy in a 3 pixel aperture radius, the mean RMS repeatability is 0.9%, which we adopted as the minimum uncertainty for the PSF photometric uncertainties.

The MIPS 24μm photometry and internal uncertainties are presented in Table 1. The S13 images were processed using a calibration factor of 0.0447 MJy sr^{-1}. Following Engelbracht et al. (2006), we adopted an calibration uncertainty of 4%.

4. MIPS 70μm

The FEPS team obtained MIPS 70μm observations for 323 sources, and data were extracted from the archive for five sources. Observations were obtained in photometry mode with an exposure time of 10 seconds, and the the number of cycles ranged between 2 and 10.

4.1. Image Processing

The MIPS 70μm images were processed with the SSC pipeline version S13 that removes the bias, subtracts a dark image, applies a flat field correction, and linearizes the pixel response. The individual BCD images were mosaicked with the Germanium Reprocessing Tools (GeRT) software package S14.0 version 1.1 developed by the SSC. The GeRT package performs column filtering on the BCD images to remove streaks in the BCD images, and then performs a time median filter to remove residual pixel response variations. A $40'' \times 40''$ region centered on the source position was excluded when computing the time and column filtering such that the filtering process is not biased by source. The filtered images were formed into mosaics using MOPEX. Outlier pixels were rejected using a 3σ clipping threshold.

4.2. Photometry

Aperture photometry was performed on the MIPS 70μm mosaics using a custom modified version of IDLPHOT. The adopted aperture radius of $16''$ was chosen to optimize the signal to noise for faint sources in the FEPS source. The sky-level was computed as the mean value of the pixels in a sky-annulus that extends from $40''$ to $60''$ after performing the iterative clipping procedure described in §2.1. The aperture radius was fixed on the expected stellar position using the WCS contained in the image headers, and no centroiding was performed. Visual inspection of the 70μm mosaics identified 19 images where a point source was located within the outer sky radius but offset from the stellar position determined from 2MASS astrometry (see also §6). For all 19 sources, a point source function (PSF) was fitted to the contaminating source and subtracted from the image using the MOPEX package. Aperture photometry was then recomputed on the PSF-subtracted image.

The 70μm photometric uncertainty is estimated from

$$\sigma = \Omega\ \Sigma_{sky}\ \sqrt{N_{ap}}\ \eta_{sky}\ \eta_{corr}\ \sqrt{1.0 + N_{ap}/N_{sky}}, \quad (1)$$

where Σ_{sky} is the RMS of the pixel values in the sky annulus in surface brightness units, Ω is the solid angle of a pixel, N_{sky} is the number of pixels in the sky annulus, N_{ap} is the number of pixels in the aperture, η_{sky} accounts for non-uniform noise between the aperture and sky annulus, and η_{corr} corrects for correlated noise between image pixels. The term η_{corr} was estimated as the ratio of the pixel size in the raw images ($\sim 10''$) to that in the mosaics ($4''$), or $\eta_{corr} = 2.5$.

The term η_{sky} accounts for non-uniform noise across the mosaics. The noise uniformity was assessed by first scaling the 70μm mosaics to a common median value. The standard deviation of each pixel in the stack of mosaic images were then computed after removing 35 images where the FEPS target was clearly detected. The resulting image showed that the mosaic noise was higher along the columns near the source position due to noisy time-variable stim latents. In addition, it was found that the noise was higher near the source position corresponding to the masked region. For the adopted target aperture and sky radius, the sky rms was 40% higher in the source aperture compared to the sky annulus. Therefore, we adopted $\eta_{sky} = 1.40$.

Figure 5 shows a histogram of the signal-to-noise ratio (SNR) for the 70μm photometry. Visual inspection of the image indicates the majority of the FEPS sources have not been detected at 70μm. Therefore, the histogram in Figure 5 should be a gaussian with unit dispersion, as shown by the solid line, if Equation 1 contains the dominant noise terms. In practice, the observed SNR distribution is broader than the expected gaussian distribution and includes SNR values as low as -4.2. The standard deviation of sources with SNR values between -4.2 and 4.2 is 1.49, and as shown by the dotted curve in Figure 5, a gaussian with a dispersion of 1.49 adequately reflects the observed distribution. The origin of the apparent excess noise is unknown, but nonetheless, we have scaled the photometric uncertainties for all sources by a factor of 1.49.

MIPS 70μm photometry is calibrated to a theoretical point-spread-function. The aperture correction needed to place the background-subtracted fluxes measured in a finite aperture on the same scale as the theoretical PSF depend on the temperature of the underlying source emission. In anticipation that the FEPS MIPS 70μm observations did not detect the stellar photosphere in most cases and that debris disks around solar-type stars have temperatures of $\sim$50-100 K, aperture corrections were measured using a 100 K PSF. The derived aperture correction for an aperture radius of $16''$ and a sky annulus between 40 and $60''$ is 1.766.

The final photometry and internal uncertainties are presented in Table 1. The adopted calibration factor is 702.0 MJy sr^{-1} / (DN s^{-1}) with an uncertainty of 7% as reported on the SSC MIPS calibration web pages.

5. Relative Calibration of IRAC and MIPS 24μm Photometry

The 24μm to 8μm flux ratio plays a prominent role in our data analysis. Since the MIPS and IRAC observations were obtained with different integration times, we examine the relative calibration between these two instruments. To search for potential affects of variable exposure

times in the instrument calibration, we selected 61 stars that have been observed with IRAC frame-times of 0.10 sec and compared the distribution of flux ratios with respect to MIPS 24μm observations independent of the IRAC frame time. NEED TO MENTION WE HAVE EXCLUDED IR EXCESS OBJECTS. In Figure 3, we plot the 24μm to 8μm flux ratio for MIPS 3 second (top panel) and 10 second (bottom panel) exposure times versus the $J-K$ color. As demonstrated in this figure, the 24μm to 8μm flux ratio for stars observed with the 3 second MIPS exposure times are lower on average by a factor of $0.972 +/- 0.008$ relative to the 10 second data. Engelbracht et al. (2006) report a similar flux offset as a function of the MIPS exposure time based on four stars. The $J-K$ colors between the two samples overlap, and therefore the difference in the flux ratios is not a result of different spectral types between the two samples. Since the MIPS calibration is tied to the 3 second exposure times (Engelbracht et al. 2006), we have applied a flux correction to the 10 second data to obtain a uniform flux scale.

After deriving a flux correction for the MIPS 10 second observations, we now consider the flux calibration observed for different IRAC exposure times. In Figure 4, we plot the 24μm to 8μm flux ratio as a function of $J-K$ color for various IRAC frame-times. The dashed line shows the mean flux ratio for the 0.40 second frame time. As shown in the figure, there are systematic differences in the mean flux ratio for the various IRAC frame-times. Formally, we find that a multiplicative scale factor of 0.971 ± 0.005 must be applied to the 0.02 second frame-time data to agree with the 0.40 second data, 1.011 ± 0.006 for the 0.10 second data, and 0.964 ± 0.005 for the 0.60 second data. We consider these correction factors preliminary since they have not yet been verified by the SSC by observing the same star with different frame-times. NEED TO MENTION THAT WE HAVE NOT RULED OUT THAT THIS IS A ASTROPHYSICAL EFFECT.

The IRAC calibrators in Reach et al. (2005) were observed in full-array mode. To test the sub-array and full-array calibration, we analyzed the observations of the star HD 135285 that were obtained by the SSC in full-array mode and in sub-array mode with 0.4 sec integration times. The mean ratio of the fluxes measured sub-array mode to the full-array mode are 1.004 ± 0.004 for IRAC channel 1, 1.001 ± 0.004 for channel 2, 0.995 ± 0.002 for channel 3, and 0.997 ± 0.001 for channel 4. The weighted mean for all four channels is 0.997 ± 0.001. We conclude that any offsets between the sub-array and full-array mode is less than 1%, and the dominant calibration uncertainty is the apparent photometric offsets for the different IRAC frame-times.

6. Confusion

The infrared background often contains emission from extended cirrus or bright point-sources which may contaminate the photometry. The contribution from these contaminants will increase toward longer wavelengths, and create the appearance of an infrared excess. Since we anticipate that the emission associated with the stellar photosphere or a circumstellar disks to be nearly point-like and centered on the star, potential contamination to the 24μm or 70μm photometry can be identified from extended emission or emission offset from the stellar position.

In Figure 6, we show the angular offsets between the 24μm positions measured from PSF fitting and the 2MASS coordinates for the star after correcting for proper motion and the epoch of observation. The 24μm coordinates where computed from the astrometric information in the image headers. Different symbols are indicated for sources with (solid circles) and without (crosses) infrared excesses to determine the relative astrometric accuracy of the two positions. Two sources have 24μm positional offsets larger than 1.8$''$, but neither exhibits an infrared excess. Excluding these two outliers, the dispersion in the right ascension and declination offsets are 0.40$''$ and 0.36$''$ respectively; stars without infrared excesses have 2-4% larger dispersion in the offsets than stars with infrared excesses. The 24μm excess source with the largest angular offset, HD 201219 at 1.3$''$, deviates by 2.4σ based on the measured dispersions.

To investigate the 70μm emission centroid relative to the photosphere, the 70μm positions where computed by fitting a two-dimensional gaussian to a 44×44$''$ (11×11 mosaicked pixels) region centered on the expected stellar position. Figure 7 shows the difference between the 70μm and 2MASS astrometry as a function of the 70μm SNR in a 16$''$ aperture. For sources with SNR $>$ 3, the positional agreement is typically better than 3$''$ for all but three sources: HD 201219 (5.1$''$offset), HD 104467 (12.8$''$), and RX J1111.7−7620 (13.4$''$). RX J1111.7−7620 is separated by 24.4$''$ from the classical T Tauri star XX Cha; these sources have comparable brightness at 70μm and the gaussian fit converged to a centroid intermediate between the two sources. HD 104467 is a single point source offset from the stellar position. Given the large offset from the expected stellar position compared to other sources with similar signal to noise ratios, we conclude the detected 70μm source is unrelated to the star. Finally, the HD 201219 70μm mosaic contains two point sources separated by 20.9$''$ that distorted the gaussian fit. The brightest of the two sources is 3.4$''$ from the 2MASS position for HD 201219. Since the latter offset is not unusual given the 70μm SNR for this source (5.9), we assume the 70μm source in fact associated with HD 201219.

To further search for contaminants in the MIPS photometry, we present the flux ratio measured in two apertures for 24μm and 70μm in Figures 8 and 9 respectively. AWKWARD SENTENCE. The dotted lines in each figure show the expected ratio from PSF measurements. At 24μm, the scatter in the flux ratio is similar for sources with and without 24μm excesses. For SNR $>$ 300, the most extreme 24μm outlier is HD 107146 at SNR=900. Other observations however have conclusively demonstrated that this source is surrounded by a circumstellar disk (Williams et al. 2004; Ardila et al. 2005; Carpenter et al. 2005). At 70μm, two sources (HD 104467 and RX J1111.7−7620) with SNR $>$ 3 have anomalously large ratios ($>$ 1.8). As discussed in §4.2, these sources have a nearby source that contaminates the photometry of the FEPS target and were PSF-subtracted before performing the final photometry.

In summary, we conclude that the astrometry and curve-of-growth for the infrared excesses sources are consistent with point source emission centered on the stellar position, and there is no compelling evidence that contaminants systematically influence the 24 and 70μm photometry. These results do not exclude the possibility that the photometry for some sources may be contaminated, but any such contaminated must be present in a minority of sources.

7. IRS Low Resolution Spectra

Low resolution spectra (R $\sim$60 – 120) were obtained with IRS (Houck et al. 2004). Data acquisition and reduction procedures are described in Bouwman et al. (2007) and are only summarized here. Targets were acquired in the spectrograph slit using a high-accuracy IRS or PCRS peak-up with a 1σ pointing uncertainty of $0.4''$ radius. Two nod positions per cycle were obtained in standard staring mode with a minimum of six cycles per target for redundancy and to allow rejection of bad pixels and cosmic ray hits. Most targets were observed between 7.7 and 35μm; beyond 35μm the spectra suffer from excess noise and cannot be used. A subset of the sources were also observed between 5.3 and 7.7μm, but these data are not analyzed here.

Five sources have incomplete wavelength coverage between 7.7 and 35μm. HD 72905 was observed only in the SL2 by the FEPS team since the longer wavelengths are observed as part of a GTO program. The peak-up observations for HII 2881 and R45 selected the incorrect source and the IRS spectra are not for the intended target. The SL1 observations for HD 13974 are centered on the incorrect target, but the longer wavelength observations are correct.

Internal uncertainties in the spectra were computed based on the scatter between adjacent pixels. A 15-pixel section of a spectrum was extracted around a given pixel position. A quadratic function was fitted to the spectrum to remove global flux-density variations with wavelength. The RMS of the residuals was then assigned as the uncertainty for that pixel. The produce was repeated for all pixels in the spectrum.

8. Stellar Properties

We now move from a description of the data reduction procedures to a description of ancillary analysis used by several FEPS programs.

8.1. Visual Extinction

Distances of the FEPS targets extend upwards of 343 pc and the extinction from the interstellar medium may be non-negligible for many applications. The visual extinction toward individual stars was estimated based on several criteria. First, stars within the Local Bubble are expected to have small extinction at visual wavelengths. The size of the Local Bubble has been measured by observing interstellar absorptions lines toward stars with known distances, and then determining the column density as a function of distance. Welsh, Crifo, & Lallement (1998) present an analysis of Na I column density measurements toward stars with Hipparcos distance estimates. The estimated visual extinction is less than 0.01 mag out to a distance of 75 pc. Therefore, we adopted an extinction of 0 mag for the 169 stars in the FEPS sample where $d + 3\sigma(d) \leq 75$ pc, where d and $\sigma(d)$ are the distance and uncertainty respectively.

The visual extinction toward the clusters in the FEPS sample have been extensively studied in the literature. For the Hyades, Taylor (2006) place an upper limit at 95% confidence of $E(B-V) = 0.001$ mag, and we therefore adopt $A_V = 0$ mag. Breger (1986) compiled spectral types and optical photometry for about 120 Pleiades members and derived $E(B-V) = 0.04$ on average, but with lower reddening to the east of the cluster (0.03 mag) compared to the west (0.06 mag). Assuming a factor of 3.1 to convert the $B-V$ reddening to visual extinction, we adopt a constant value of 0.12 mag for the Pleiades stars. Following Pinsonneault et al. (1998), we adopt an average $E(B-V) = 0.10$ (see Crawford & Barnes 1974; Prosser 1994), or $A_V = 0.31$ mag, for Alpha Per. Finally, for IC 2602, we adopt a visual extinction of 0.12 mag (Whiteoak 1961)

Many of the FEPS stars are field objects with distances larger than 75 pc. The visual extinction for these stars was assigned based on published spectral types and the observed color excess. Spectral types are available for 300 of the 328 FEPS sources (see Hillenbrand et al. 2007, for details). Optical (Johnson B and V, Tycho B and V) and near-infrared (2MASS J, H, and K_s) colors where compiled from the literature for most FEPS sources. For 41 sources sources, the FEPS project obtained B and V photometry using the 61″ Kuiper and 0.9 m CTIO telescopes (N. Crockett, private communication), and was transformed to the Johnson photometric system.

The intrinsic colors as a function of spectral type were compiled from the literature by cross-correlating the Hipparcos catalog with the Michigan Spectral Catalog, Tycho-2, and 2MASS. The positional match between the Tycho-2 and Michigan spectral atlas from Wright et al. (2003) was used as a starting pointing. Only 2MASS sources with a PH_QUAL flag of AAA and a confusion flag of 000 were used. Finally, a photometric uncertainty less than 0.073 was required in each photometric band. The average color was then computed as a function of spectral type for stars within 75 pc for B and V photometry, and within 100 pc for colors involving J, H, and K_s. In computing the average colors, individual measurements were weighted by the variance of the measurements, and outliers from poor photometry or spectral types were removed using an iterative sigma-clipping procedure. Table 2 list the intrinsic colors adopted when computing the color excess.

The color excess was computed from the observed $(B-V)_{\rm Johnson}$, $(B-V)_{\rm Tycho}$, $V_{\rm Tycho} - K_{\rm s}$, and $J - K_{\rm s}$ colors and the intrinsic colors listed in Table 2. The intrinsic $(B-V)_{\rm Johnson}$ colors were computed from the $(B-V)_{\rm Tycho}$ colors and the Tycho-to-Johnson transformation equations in Mamajek, Meyer, & Liebert (2002, 2006). The visual extinction was estimated for each color using the extinction law compiled by Mathis (1990), and the weighted mean was adopted as the extinction.

For 9 stars, the visual extinction could not be estimated using the above techniques since either a spectral type was not available, or the computed extinction was unphysical (i.e. $A_V < 0$ mag). In the latter case, it is presumed that the photometry was poor or the spectral type is erroneous. For these stars, we estimated the extinction using the Sandage (1972) extinction model assuming an exponential disk (see Chen et al. 1998).

9. Surface Gravity and Stellar Effective Temperature

The temperature and surface gravity of the stars are needed in fitting the Kurucz model atmospheres as described in §10. This section summarizes the procedure to estimate these properties for the FEPS sample. The procedure depends on the stellar age, as solar-mass stars young than ~ 100 Myr are contracting toward the main sequence and the surface gravity varies with time.

Stars older than 100 Myr in the FEPS sample were considered to main-sequence stars and were assigned a surface gravity of $logg = 4.50$ g cm^{-2}. Stellar effective temperatures were estimated using the $B-V$ and $V-K$ versus temperature relations derived by Houdashildt, Bell, & Sweigart (2000) after dereddening the observed photometry using the extinction values derived in §8.1. If the temperature uncertainty derived from the photometry is larger than 130 K, the temperature was instead computed from a temperature vs. spectral type relation using the colors listed in Table 2, the Tycho to Johnson color transformations from Mamajek, Meyer, & Liebert (2002, 2006), and the Houdashildt, Bell, & Sweigart (2000) color-temperature relations. A limit of 130 K was adopted since that is approximately the temperature uncertainty associated with 2 spectral subclasses.

Solar-type stars younger than 100 Myr will be contracting toward the main sequence and will generally have lower surface gravities. Derivation of the surface gravities and effective temperatures need to be solved jointly. First, the effective temperature was computed assuming the star is on the main sequence. The surface gravity was then estimate from the D'Antona & Mazzitelli (1997) pre-main-sequence evolutionary tracks using the derive temperature and assumed age from (Hillenbrand et al. 2007). If the temperature was estimated from the spectral type, an iterative correction needs to be applied since the derived temperature depends on both the spectral type and surface gravity. For the estimate surface gravity, a new temperature and was derived using the effective temperature as a function spectral type and surface gravity relation in Gray (1992). With the new temperature, the surface gravity was re-derived from the D'Antona & Mazzitelli (1997) evolutionary tracks.

10. Model Photospheres

In several FEPS studies, the observed *Spitzer* fluxes have been compared to model photospheric fluxes to infer the presence of an infrared excess diagnostic of circumstellar disks. The model flux was estimated either by fitting Kurucz model atmospheres to optical and near-infrared photometry and extrapolating the model to longer wavelengths, or by examining the flux ratios between mid-infrared and or using flux ratios. This section describes the procedure to compute model fluxes from Kurucz model atmospheres.

10.1. Optical and Near-infrared Photometry

The Kurucz models were normalized to published optical and near-infrared photometry. Photometric catalogs incorporated for this study include Tycho-2 (Høg et al. 2000), Hipparcos (Perryman et al. 1997), 2MASS, the General Catalogue of Photometric Data (GCPD; Mermilliod, Mermilliod, & Hauck 1997). The GCPD is a compilation of published ground based observations that includes, among others, *UBV* Johnson, *RI* Cousins and Kron, and Stromgren *uvby*. These data are of non-uniform quality compared to these other surveys. Ground based infrared photometry from the ISO preparatory observations were downloaded[4] in both the ESO and Tenerife photometric systems

10.2. Synthetic Photometry

Synthetic colors were computed from Kurucz models[5] with convective overshoot and turbulent velocity of 1 km s^{-1}. For wavelengths longer than 10μm, the Kurucz models are sampled at 10.02μm, and then between 20 and 160μm in steps of 20μm. For wavelengths longer than 10μm, the Kurucz models were resampled at finer wavelengths by interpolating between model data points assuming a $S_\nu \propto \nu^2$ spectrum. s Synthetic fluxes can be computed by convolving a Kurucz model atmosphere with the spectral response of a given photometric system. The spectral response, $T(\lambda)$, includes the quantum efficiency of the detector and the transmission of both the atmosphere (if appropriate) and filter. The product of these three transmission functions for any given band will be referred to as a FAD (i.e. filter + atmosphere + detector).

By definition, the bandwidth of the filter in wavelength and frequency units can be computed as

$$\Delta\lambda = \int T(\lambda)d\lambda/T_{\rm max} \quad (2)$$

$$\Delta\nu = \int T(\lambda)d\nu/T_{\rm max}, \quad (3)$$

where $T_{\rm max}$ is the peak transmission. The quoted uncertainties in the band widths were computed by assuming a 5% uncertainty in the transmission at any given wavelength. The spectral irradiance can be computed by integrating the spectrum, $S(\lambda)$, over the FAD as

$$I = \int S(\lambda)T(\lambda)d(\lambda). \quad (4)$$

The corresponding flux density is then defined as

$$S_\lambda = I/\Delta\lambda \quad (5)$$

$$S_\nu = I/\Delta\nu. \quad (6)$$

[4]http://www.iso.vilspa.esa.es/users/expl_lib/ISO/wwwcal/isoprep/gbpp/photom/

[5]http://kurucz.harvard.edu

Since optical and near-infrared fluxes are typically quoted in magnitudes, the synthetic fluxes further need to be converted appropriately based on the flux for a zero-magnitude star as

$$m = -2.5 \log \left(\frac{S_\lambda}{ZP} \right) + zpo, \tag{7}$$

where ZP is the zero point of the system, and zpo is the offset needed to convert the synthetic photometry to the observed photometric system. Martin Cohen and collaborators have produced a series of papers to define the zero points and zero point offsets, as well the bandwidth and wavelengths, and many photometric systems. In particular, we adopted the calibration by Cohen et al. (2003a) for 2MASS, Cohen, Wheaton, & Megeath (2003ab) for Tycho-2, Hipparcos, and Landolt BVRI, and Cohen et al. (1999) for ESO HK and Tenerife HK. Finally, for Stromgren photometry, we adopted the calibration... AND

10.3. Fitting Procedure

The χ^2 merit equation to determine the best fit model is

$$\begin{aligned} \chi^2 &= \sum_{i=1}^{N} \frac{[F_i(obs) - F_i(model, T_{eff}, A_V, [Fe/H], logg, \Omega)^2}{\Delta F_i(obs)^2 + \Delta F_i(model)]^2} \\ &+ \left(\frac{T_{eff} - T_{eff}(SpT, log\ g)}{\sigma_{Teff}(SpT, log\ g)} \right)^2, \end{aligned} \tag{8}$$

where $F_i(obs)$ is the observed flux typically expressed in magnitudes, $F_i(model)$ is the model flux that depends on the stellar effective temperature (T_{eff}), visual extinction, metallicity, surface gravity, and solid angle (Ω), and $T_{eff}(SpT, logg)$ is the nominal temperature of the star given the spectral type and surface gravity.

Equation 8 was minimized using a modified version of the Levenberg-Marquardt method as implemented by the LMDIF routine in the MINPACK library. The model parameters are the solid angle of the star, the effective temperature, surface gravity, metallicity, and visual extinction. The metallicity was fixed to [Fe/H]=0.13 for the Hyades stars following the measurements from (Paulson, Sneden, & Cochran 2003) and [Fe/H]=0 for all other stars. The constraints in the fitting procedure are that the solid angle of the star has a positive value, and the visual extinction is non-negative. If the star has a distance within 0 pc such that it is within the Local Bubble, the extinction was fixed at 0 mag. Photometry at wavelengths between 0.4 and 2.5μm was used in the fit. Shorter wavelength photometry, in particular U-band observations, were omitted, since those data are difficult to calibrate from the ground and sensitivity to the stellar metallicity. Longer wavelengths were omitted to avoid having infrared excesses contaminate the fitting procedure.

Uncertainties in the model fluxes were computed using a grid search around the best-fit model parameters. The size of the grid was ± 3 times the nominal parameter uncertainties computed the covariance matrix. For each point in the grid, the χ^2 between that model and the observed fluxes

was computed, as well as the model fluxes in the *Spitzer* IRAC and MIPS photometric bands. The relative probability that the grid point can reproduce the observations is $e^{-\chi^2/2}$. By computing the probabilities and model fluxes over all grid points, the probability distribution of the model fluxes can be constructed.

Since it is not feasible to present the full probability distribution for each *Spitzer* photometric band and each star. We therefore characterize the full probability distribution for a photometric band by the nominal flux, F_{model}, and the 1σ uncertainty ΔF_{model}. The nominal flux is is given by the flux computed from the best fit model parameters. The 1σ flux uncertainty is defined as the smallest range of model fluxes about F_{model} that encompass 68% of the total probability. INDICATE WHERE THE MODELS ARE LOCATED AND CAVEATS : SPOTS, binaries, bad photometry

11. Summary

The FEPS *Spitzer* Legacy program is designed to obtain carefully measured spectral energy distributions for over 300 solar-type stars spanning ages between 3 Myr and 3 Gyr. The goal of the program is to measure the incidence and evolution of circumstellar disks with time to place our Solar System in context.

We have described the data reduction procedures adopted by the FEPS team to obtain accurately and well-characterized photometry and spectra. The image processing steps for the IRAC and MIPS data closely follow the data reduction procedures recommended by the *Spitzer* Science Center and the *Spitzer* Instrument Teams. Using customized versions of existing data reduction packages to automate photometric measurements of 328 stars, we achieved repeatability better than 1.2% in IRAC channels 1, 2, and 4. Not finished...

JMC would like to thank Dave Frayer and the staff at the *Spitzer* Science Center for patiently answering numerous questions regarding *Spitzer* data. This work is based on observations made with the *Spitzer Space Telescope*, which is operated by JPL/Caltech under a contract with NASA. The program made use of data and resources from the FEPS project, which receives support from NASA contracts 1224768, 1224634, and 1224566 administered through JPL. This research made use of the SIMBAD database, operated at CDS, Strasbourg, France. This paper made use of data products from the Two Micron All Sky Survey, which is a joint project of the U. Massachusetts and the Infrared Processing and Analysis Center/Caltech, funded by NASA and the NSF.

REFERENCES

Ardila, D. R. et al. 2005, ApJ, 617, L147

Bouwman et al. 2007, ApJ, submitted

Breger, M. 1986, ApJ, 309, 311

Carpenter, J. M., Wolf, S., Schreyer, K., Launhardt, R., & Henning, T. 2005, AJ, 129, 1049

Chen, B., Vergely, J. L., Valette, B., & Carraro, G. 1998, A&A, 336, 137

Cohen, M., Megeath, S. T., Hammersley, P. L., Martín-Luis, F., & Stauffer, J. 2003a, 125, 2645

Cohen, M., Walker, R. G., Carter, B., Hammersley, P. L., Kidger, M., & Noguchi, K. 1999, AJ, 117, 1864

Cohen, M., Wheaton, W. A., & Megeath, S. T. 2003b, AJ, 126, 1090

Crawford, D., & Barnes, J. 1974, AJ, 79, 687

D'Antona, F., & Mazzitelli, I. 1997, MmSAI, 68, 807

Engelbracht et al.2006, in press

Evans, N. J., II, et al. 2003, PASP, 115, 965

Fazio, G., Hora, J. L, Allen, L. E., et al. 2004, ApJS, 154, 10

Gray, D. F. 1992, The Observation and Analysis of Stellar Photospheres (Cambridge: Cambridge Univ. Press)

Hillenbrand, L. A., et al. 2007, in preparation

Hines, D. C., et al. 2006, ApJ, 638, 1070

Hollenbach, D., et al. 2005, ApJ, 631, 1180

Høg, E., Fabricius, C., Makarov, V. V., Urban, S., Corbin, T., Wycoff, G., Bastian, U., Schwekendiek, P. & Wicenec, A. 2000, A&A, 355, L27

Houk, J. et al. 2004, ApJS, 154, 18

Houdashildt, M. L., Bell, R. A., & Sweigart, A. V. 2000, AJ, 119, 1448

Kim, J. S., et al. 2005, ApJ, 632, 659

Makovoz, D., & Marleau, F. R. 2005, PASP, 117, 1113

Mamajek, E. E., Meyer, M. R., & Liebert, J. 2002, AJ, 124, 1670

Mamajek, E. E., Meyer, M. R., & Liebert, J. 2006, AJ, 131, 2360

Mathis, J. S. 1990, ARA&A, 27, 37

Mermilliod, J.-C., Mermilliod, M., & Hauck, B. 1997, A&AS, 124, 349

Metchev, S., & Hillenbrand, L. A. 2006, in preparation

Meyer, M. R., et al. 2005, ApJS, 154, 422

Meyer, M. R. et al. 2006, PASP, 118, 1690

Pascucci, I. et al. 2006, ApJ, 651, 1177

Pascucci, I. et al. 2007, in preparation

Paulson, D. B., Sneden, C., Cochran, W. D. 2003, AJ, 125, 3185

Perryman, M. A. C., et al. 1997, A&A, 323, L49

Pinsonneault, M. H., Stauffer, J., Soderblom, D. R., King, J. R., & Hanson, R. B. 1998, ApJ, 504, 170

Prossser, C. F. 1994, AJ, 103, 488

Reach, W. T., et al. 2005, PASP, 117, 978

Rieke, G. et al. 2004, ApJS, 154, 25

Sandage, A. 1972, ApJ, 178, 1

Silverstone, M. D., et al. 2006, ApJ, 639, 1138

Taylor, B. J. 2006, AJ, 132, 2453

Welsh, B. Y., Crifo, F., & Lallement, R. 1998, A&A, 333, 101

Werner, M., Roellig, T., Low. F., et al. 2004, ApJS, 154, 1

Whiteaok, J. B. 1961, MNRAS, 123, 245

Williams, J. P., Najita, J., Liu, M. C., Bottinelli, S., Carpenter, J. M., Hillenbrand, L. A., Meyer, M. R., & Soderblom, D. R. 2004, ApJ, 604, 414

Wright, C. O., Egan, M. P., Kraemer, K. E., & Price, S. D. 2003, AJ, 125, 349

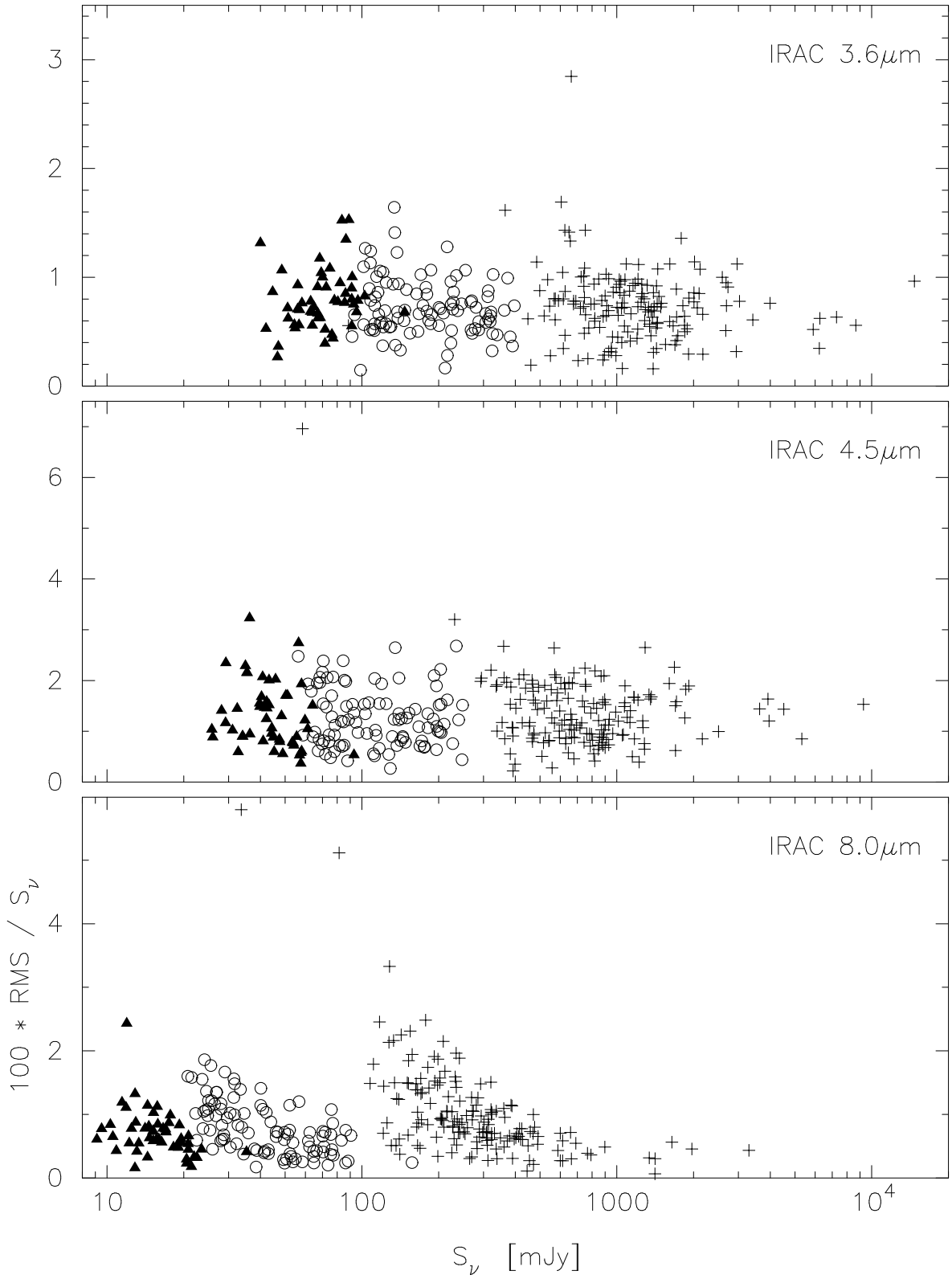

Fig. 1.— The normalized RMS from the four subarray dither positions plotted versus the mean flux for the FEPS IRAC subarray data. IRAC frame-times of 0.02, 0.1, and 0.4 sec are represented by crosses, open circles, and filled triangles respectively. As described in the text, we used the repeatability between the dithers to assign a minimum photometric uncertainty of 0.72%, 1.22%, and 0.66% for IRAC channels 1, 2, and 4 respectively.

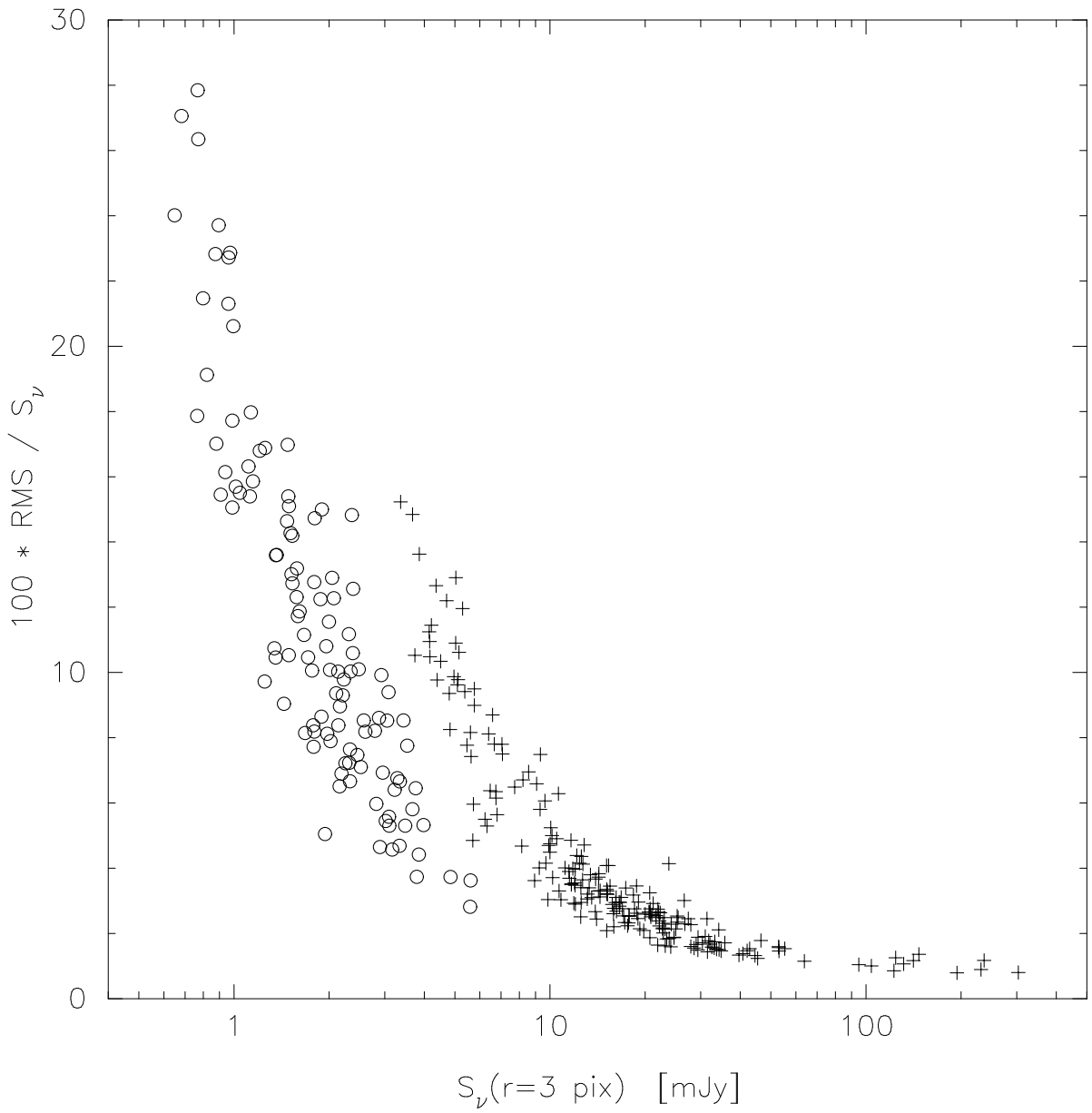

Fig. 2.— RMS repeatability of the MIPS 24μm aperture photometry measured in a 3 pixel radius on individual BCD images. Crosses represent sources observed with an exposure time of 3 sec, and open circles with 10 sec. The larger percent RMS toward fainter fluxes for a given exposure time indicates photon statistics dominate the photometric uncertainty for the fainter sources. We adopt a minimum uncertainty of 0.9% based on the mean repeatability for stars brighter than 100 mJy.

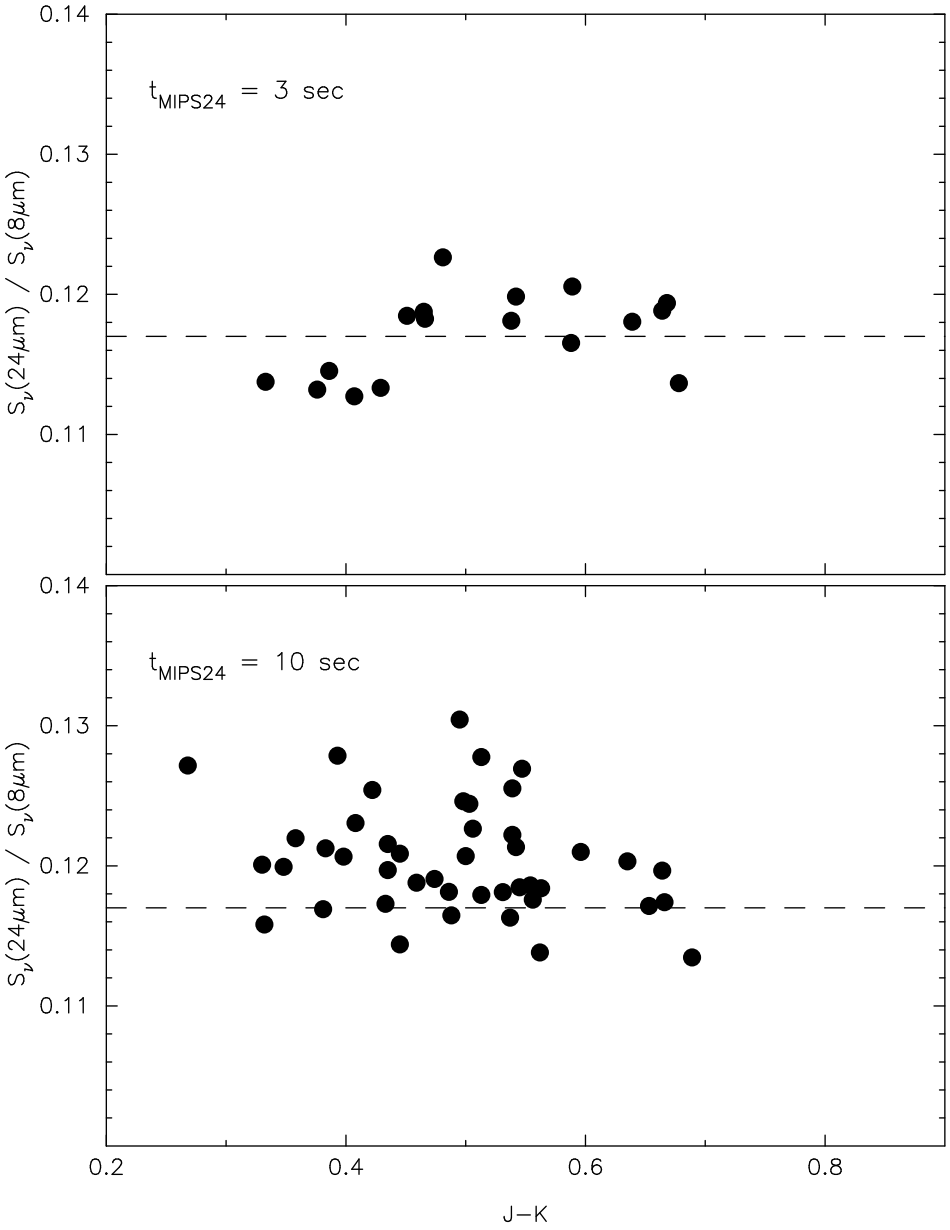

Fig. 3.— The 24μm to 8μm flux ratio plotted as a function of the $J-K$ color for stars observed with a 0.10 sec IRAC frame time. The top panel shows the results for the 3 sec MIPS 24μm exposure times and the bottom panel for the 10 sec exposure times. The dashed line shows the mean flux ratios for the 3 sec MIPS data. These results show that there is a systematic offset in the flux ratio for the different MIPS exposure times, and suggest that the fluxes measured in the 3 sec exposure times are systematically lower than those measured in the 10 sec exposure times by a factor of 0.028 ± 0.008.

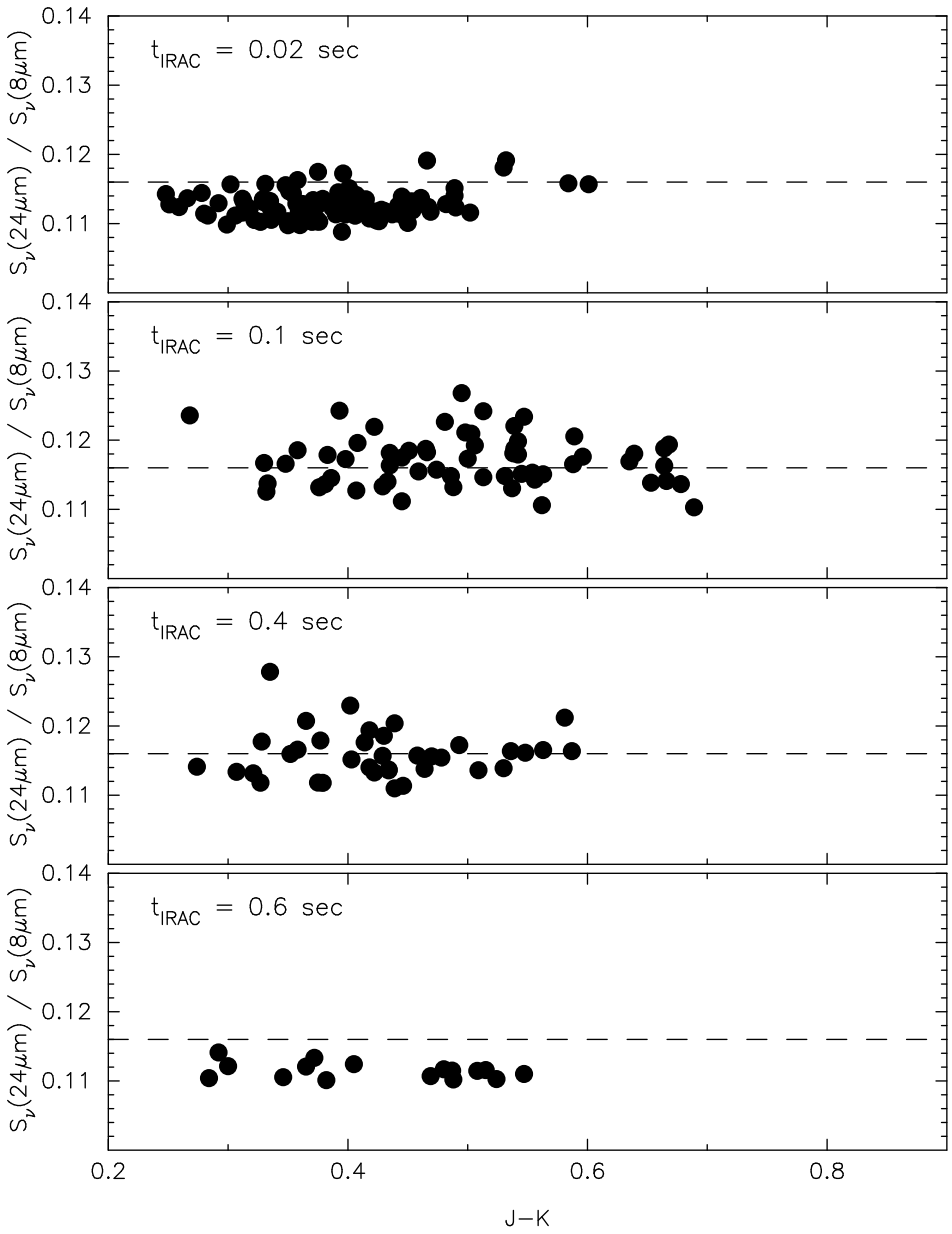

Fig. 4.— The 24μm to 8μm flux ratio plotted as a function of the $J-K$ color for various IRAC frame-times. A calibration offset to the MIPS 24μm data have been applied (see Fig. 3). The dashed line in each panel shows the mean flux ratio for the 0.40 second IRAC data. These results indicate that there are systematic variations in the 24μm to 8μm flux ratio for the various IRAC frame times.

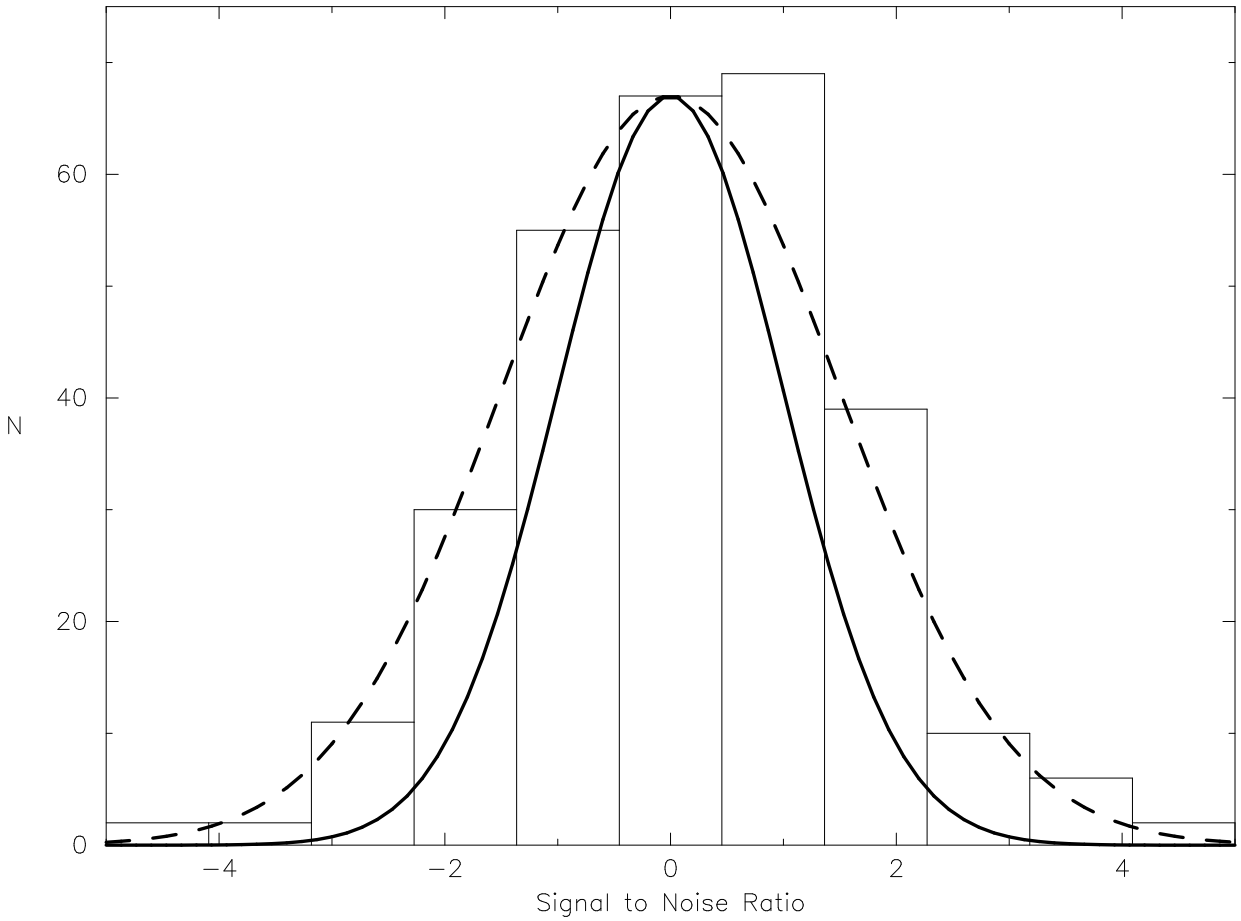

Fig. 5.— Histogram of the 70μm signal-to-noise ratio for the FEPS sources. The solid curve shows the expected signal-to-noise distribution for gaussian noise (dispersion = 1.0) that has been scaled to a peak value of N=67. The dotted line shows a gaussian with a dispersion of 1.5, which provides a better fit to the observed distribution. These results suggest that the 70μm photometric uncertainties are underestimated by a factor of 1.5, and all of the uncertainties have been scaled by this factor.

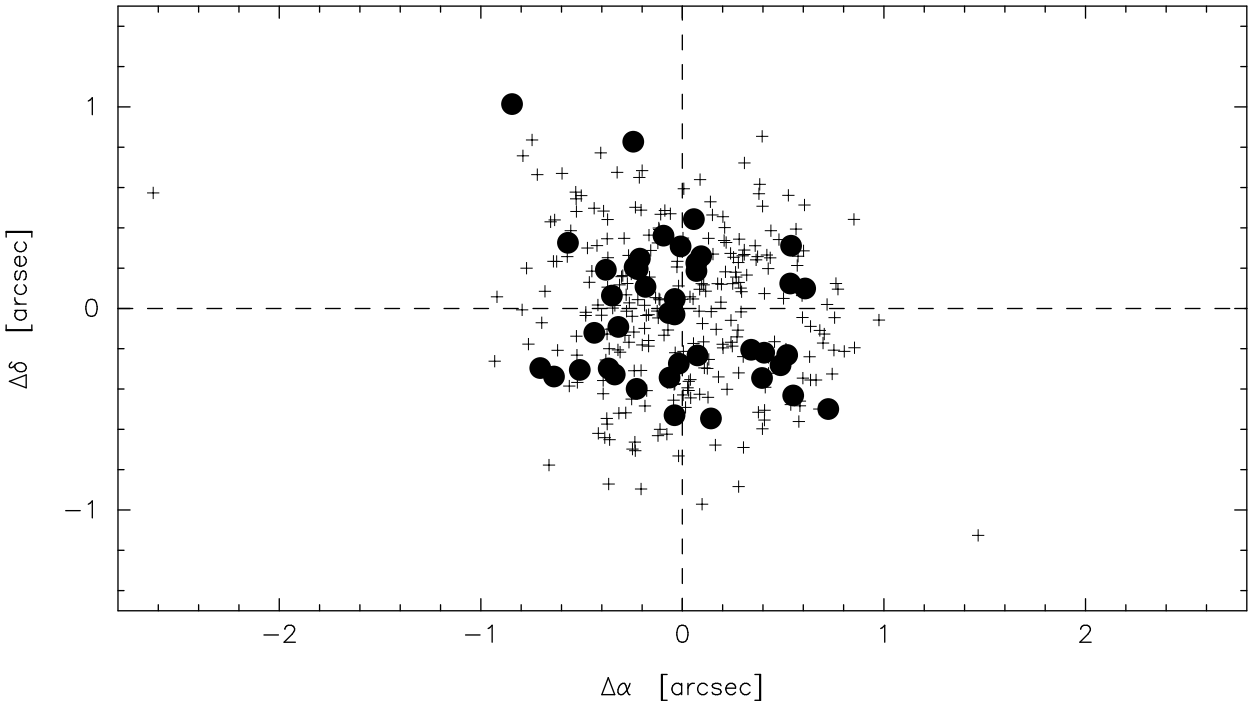

Fig. 6.— Angular offset between the 24μm emission centroid for the FEPS sources and the 2MASS position after correction for proper motion and epoch of observations. Filled circles represent sources with a $> 3\sigma$ 24μm excess and confirmed by the IRS spectrum. Crosses represent sources without a detectable 24μm excess.

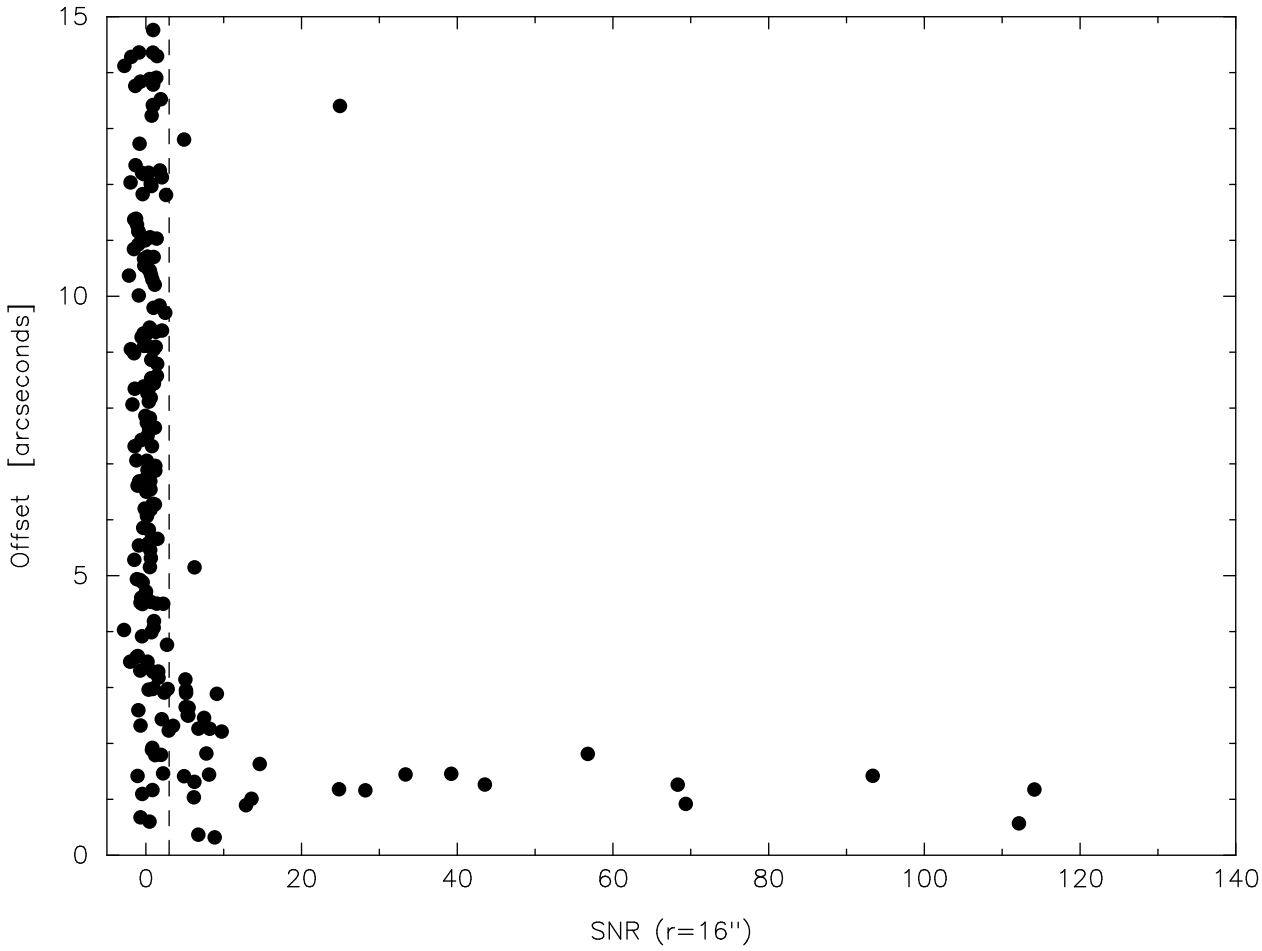

Fig. 7.— The difference between the 70μm source position and the 2MASS stellar position as a function of the 70μm signal-to-noise ratio. The 70μm centroid was estimated by fitting a two-dimensional gaussian to a $44\times44''$ region centered on the stellar position.

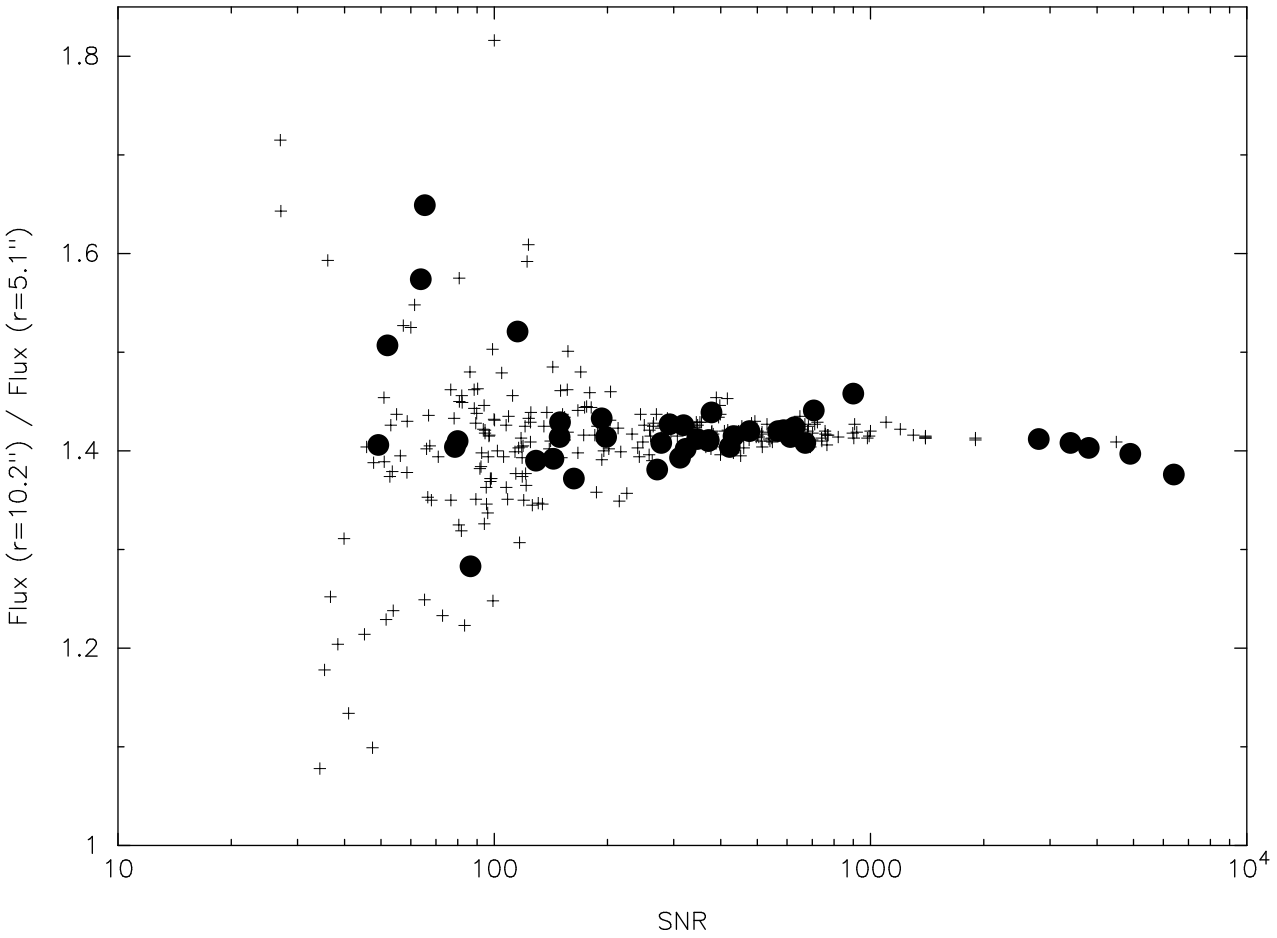

Fig. 8.— Ratio of the 24μm flux density measured in a 10.2″ aperture to that in a 5.1″ aperture as a function of the signal-to-noise ratio of the 24μm PSF photometry. Filled symbols represent sources with a $\geq 3\sigma$ 24μm excess confirmed by the IRS spectrum, and crosses indicate sources without detectable 24μm excesses.

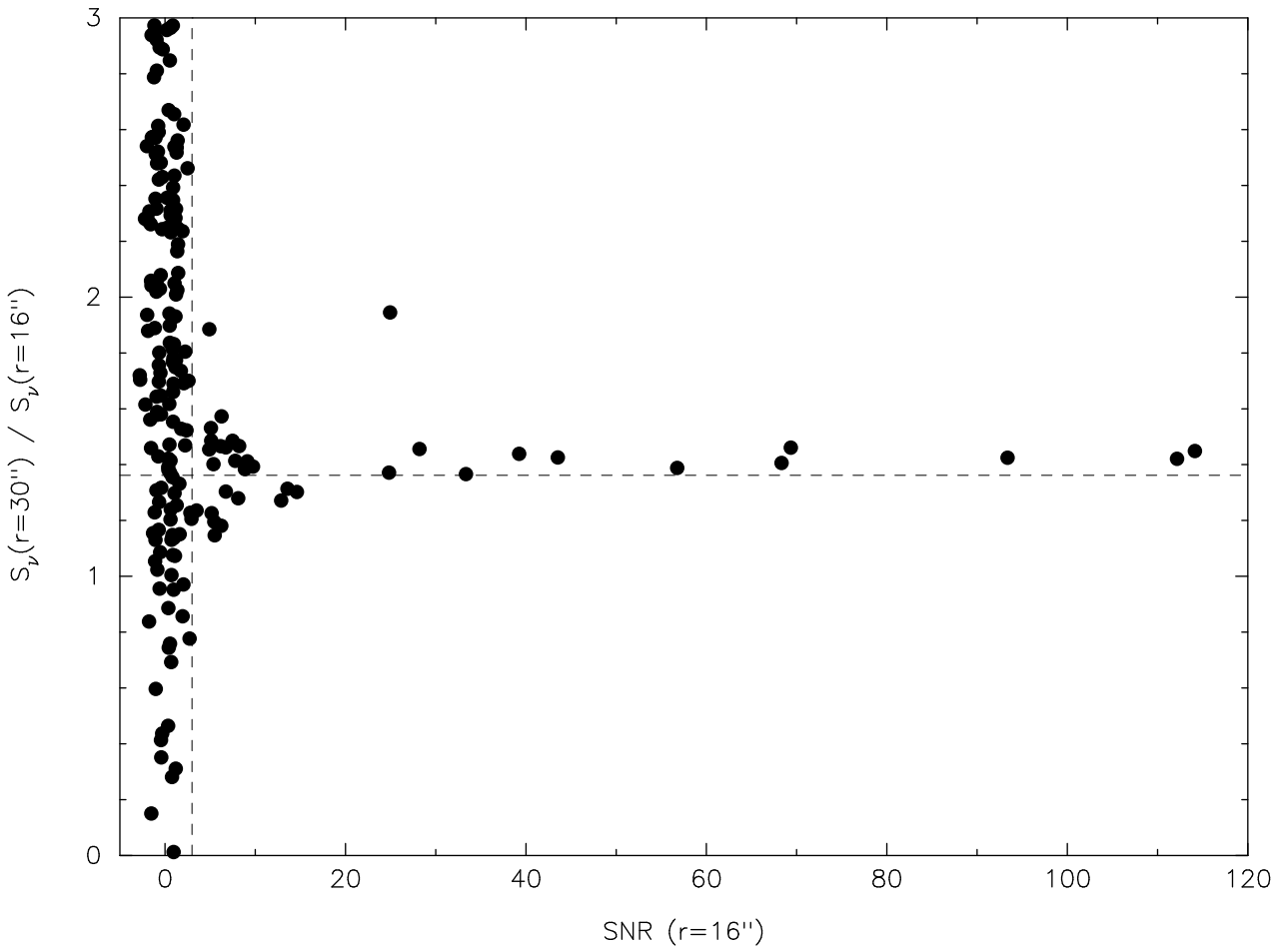

Fig. 9.— Ratio of the 70μm flux measured in a 35$''$ radius aperture to that in a 16$''$ radius aperture as a function of the signal to noise ratio. The vertical dashed line is drawn at SNR=3. The dotted line shows the expected ratio of 1.36 for a theoretical point-source with a temperature of 100 K. The two sources with SNR > 3 and flux ratios greater than 1.8 have a nearby source that partially overlap the aperture. These two contaminating sources were PSF-subtracted before performing the final photometry.

Table 1. IRAC and MIPS Photometry

Source	IRAC 3.6μm		IRAC 4.5μm		IRAC 8μm		MIPS 24μm		MIPS 70μm		IRAC	MIPS 24μ
	S_ν (Jy)	$\sigma_{\rm int}$ (Jy)	S_ν (Jy)	$\sigma_{\rm int}$ (Jy)	S_ν (Jy)	$\sigma_{\rm int}$ (Jy)	S_ν (Jy)	$\sigma_{\rm int}$ (Jy)	S_ν (Jy)	$\sigma_{\rm int}$ (Jy)	frame time (sec)	DCE Tim (sec)
1E0307.4 + 1424	91.21	0.66	57.60	0.70	20.51	0.14	2.60	0.03	-10.8	5.4	0.40	9.96
1E0324.1 − 2012	86.59	0.62	55.47	0.68	19.53	0.13	2.50	0.02	-1.7	3.7	0.40	9.96
1RXSJ025216.9 + 361658	321.18	2.31	202.24	2.47	77.25	0.51	8.81	0.08	-0.6	4.3	0.10	9.96
1RXSJ025751.8 + 115759	121.01	0.87	76.26	0.93	27.93	0.18	3.27	0.04	1.3	5.4	0.10	9.96
1RXSJ030759.1 + 302032	313.33	2.26	196.62	2.40	71.77	0.47	8.13	0.08	2.0	5.0	0.10	2.62
1RXSJ031644.0 + 192259	55.94	0.40	35.50	0.43	12.87	0.09	1.57	0.03	-9.4	5.9	0.40	9.96
1RXSJ031907.4 + 393418	47.01	0.34	29.19	0.36	10.88	0.07	1.31	0.02	-3.0	4.3	0.40	9.96
1RXSJ034423.3 + 281224	389.93	2.81	246.84	3.01	88.38	0.58	10.01	0.09	-0.4	5.5	0.10	2.62
1RXSJ035028.0 + 163121	107.74	0.78	68.39	0.83	24.39	0.16	2.95	0.03	-10.1	6.6	0.10	9.96
1RXSJ043243.2 − 152003	106.89	0.77	66.74	0.81	23.97	0.16	2.92	0.03	-2.4	3.5	0.10	9.96
1RXSJ051111.1 + 281353	223.49	1.61	139.47	1.70	53.61	0.35	7.77	0.07	1.4	11.0	0.10	2.62
1RXSJ053650.0 + 133756	179.78	1.29	112.07	1.37	41.56	0.27	4.93	0.04	-0.2	11.0	0.10	9.96
2REJ0255 + 474	396.39	2.85	248.21	3.03	90.62	0.60	10.30	0.09	-1.3	4.6	0.10	2.62
AO Men	568.24	4.09	359.74	4.81	130.52	0.86	16.16	0.15	4.9	3.4	0.02	2.62
AP 93	56.05	0.40	34.91	0.43	12.96	0.09	1.62	0.02	5.3	10.2	0.40	9.96
B102	88.83	0.68	56.44	0.77	20.52	0.14	2.54	0.11	-15.0	22.1	0.40	9.96
BPM 87617	234.87	1.69	148.05	1.81	54.85	0.36	6.59	0.06	-3.0	4.3	0.10	2.62
HD 105	1022.72	7.36	645.37	7.87	230.66	1.52	28.29	0.25	141.2	10.4	0.02	2.62
HD 377	1029.07	7.41	648.56	7.91	234.70	1.67	36.58	0.33	162.0	12.6	0.02	2.62
HD 691	967.52	6.97	597.48	7.29	218.32	1.44	25.01	0.23	8.3	7.2	0.02	2.62
HD 984	1050.29	7.56	662.15	8.08	236.77	1.56	26.88	0.24	-9.4	8.4	0.02	2.62
HD 6434	952.27	6.86	603.33	7.36	215.10	1.42	23.95	0.22	8.0	7.4	0.02	2.62
HD 6963	1211.31	8.72	752.85	9.19	271.46	1.79	32.53	0.29	44.0	8.0	0.02	2.62
HD 7661	1428.00	10.28	887.28	10.82	322.51	2.13	36.03	0.32	4.4	7.9	0.02	2.62
HD 8907	1918.20	13.81	1223.73	14.93	427.28	2.82	51.28	0.46	247.4	9.3	0.02	2.62
HD 8941	2006.73	14.45	1266.43	15.45	448.80	2.96	49.89	0.45	4.5	9.3	0.02	2.62
HD 9472	1088.63	7.84	678.21	8.27	242.00	1.60	27.28	0.25	1.1	9.5	0.02	2.62
HD 11850	952.41	6.86	595.66	7.27	211.74	1.78	24.05	0.22	-4.0	9.6	0.02	2.62
HD 12039	747.34	5.38	470.88	5.75	170.38	1.13	25.65	0.23	3.5	8.1	0.02	2.62
HD 13382	1391.67	10.02	881.73	10.76	313.35	2.07	36.27	0.33	3.2	9.5	0.02	2.62
HD 13507	1715.75	12.35	1071.21	13.07	389.82	2.57	42.99	0.39	4.4	7.4	0.02	2.62
HD 13531	1552.04	11.18	964.04	11.76	349.37	2.31	39.14	0.35	1.8	8.0	0.02	2.62
HD 13974	14705.79	105.88	9279.19	113.21	3299.77	21.78	374.1	3.40	46.0	9.0	0.02	2.62
HD 15526	182.75	1.32	113.77	1.39	40.84	0.27	4.89	0.04	-4.5	3.9	0.10	9.96
HD 17925	7280.60	52.42	4520.57	55.15	1644.56	10.85	193.6	1.70	57.0	11.6	0.02	2.62
HD 18940	1815.57	13.07	1130.20	13.79	405.23	2.67	45.58	0.41	-4.7	9.9	0.02	2.62
HD 19019	1664.30	11.98	1050.85	12.82	371.56	2.45	42.21	0.38	3.9	10.3	0.02	2.62
HD 19668	605.66	5.12	382.24	4.66	134.35	1.01	18.74	0.17	-2.0	9.2	0.02	2.62
HD 21411	1008.04	7.26	627.22	7.65	225.56	1.49	25.14	0.23	3.8	7.6	0.02	2.62
HD 22179	311.69	2.24	196.20	2.39	71.03	0.47	11.10	0.10	35.9	10.3	0.10	2.62
HD 25300	649.30	4.67	398.75	4.87	152.33	1.41	18.61	0.17	0.7	4.8	0.02	2.62
HD 25457	6259.72	45.07	3956.34	48.27	1412.34	9.32	205.8	1.90	307.2	9.2	0.02	2.62
HD 26182	227.33	1.64	144.51	1.76	52.11	0.34	5.94	0.07	1.6	8.8	0.10	2.62
HD 26990	1286.97	9.27	804.17	9.81	289.30	1.91	32.75	0.29	9.4	9.0	0.02	2.62

Table 1—Continued

Source	IRAC 3.6μm		IRAC 4.5μm		IRAC 8μm		MIPS 24μm		MIPS 70μm		IRAC	MIPS 24μm	AORKE	
	S_ν (Jy)	$\sigma_{\rm int}$ (Jy)	S_ν (Jy)	$\sigma_{\rm int}$ (Jy)	S_ν (Jy)	$\sigma_{\rm int}$ (Jy)	S_ν (Jy)	$\sigma_{\rm int}$ (Jy)	S_ν (Jy)	$\sigma_{\rm int}$ (Jy)	frame time (sec)	DCE Time (sec)	IRAC	M
HD 27466	883.45	6.36	557.40	6.80	198.51	1.31	21.90	0.20	1.7	7.6	0.02	2.62	5411584	54
HD 28495	1463.51	10.54	911.59	11.12	331.19	2.19	38.13	0.34	-7.0	10.3	0.02	2.62	5366016	53
HD 29231	1332.22	9.59	821.42	10.02	297.62	1.96	33.14	0.30	3.8	7.2	0.02	2.62	5405696	54
HD 31143	900.01	6.48	556.10	6.78	203.33	1.34	22.69	0.20	2.9	7.8	0.02	2.62	5401088	54
HD 31281	271.15	1.95	171.58	2.09	62.45	0.41	7.43	0.09	9.6	13.4	0.10	2.62	5254912	52
HD 31392	1431.93	10.31	891.69	10.88	321.84	2.12	36.88	0.33	81.6	8.4	0.02	2.62	5398016	53
HD 31950	130.03	0.94	83.02	1.01	29.00	0.24	3.69	0.04	-2.7	8.9	0.10	9.96	5303808	53
HD 32850	1487.55	10.71	929.44	11.34	336.42	2.22	38.37	0.35	2.2	11.9	0.02	2.62	5402624	54
HD 35850	3030.34	21.82	1917.88	23.40	690.67	4.56	83.52	0.75	40.3	7.5	0.02	2.62	5446912	54
HD 37006	740.10	5.33	465.45	5.68	164.16	1.08	18.64	0.17	-2.1	6.2	0.02	2.62	5388800	53
HD 37216	1122.32	8.08	694.71	8.47	250.81	1.66	28.03	0.25	6.7	9.3	0.02	2.62	5386496	53
HD 37484	893.68	6.43	568.11	7.50	202.23	1.59	54.59	0.49	114.4	7.8	0.02	2.62	5306624	53
HD 37572	1362.34	9.81	848.38	10.35	310.18	2.05	35.26	0.32	5.7	7.6	0.02	2.62	6601472	65
HD 37962	883.69	6.36	553.46	6.75	198.17	1.45	22.62	0.20	16.5	7.4	0.02	2.62	5412352	54
HD 38207	286.99	2.07	181.35	2.21	64.62	0.43	16.46	0.15	184.6	4.7	0.10	2.62	5363200	53
HD 38529	5893.09	42.43	3634.04	44.34	1339.97	8.84	149.6	1.30	75.3	11.2	0.02	2.62	5436928	54
HD 38949	775.76	5.58	488.07	5.95	172.26	1.16	20.02	0.18	7.2	8.0	0.02	2.62	5339648	53
HD 40647	872.61	6.28	543.42	6.63	195.98	1.29	22.11	0.20	7.0	6.7	0.02	2.62	5384192	53
HD 41700	2693.24	19.39	1696.38	20.70	613.28	4.05	71.78	0.65	22.2	7.6	0.02	2.62	5365248	53
HD 43989	719.52	5.18	454.19	5.54	163.22	1.21	21.14	0.19	7.1	9.8	0.02	2.62	6600704	65
HD 44594	2593.89	18.68	1606.66	19.60	587.33	3.88	63.92	0.58	5.3	6.7	0.02	2.62	5444608	54
HD 45270	2675.06	19.26	1698.63	20.72	599.85	3.96	70.18	0.63	8.5	6.0	0.02	2.62	6601216	65
HD 47875	364.71	2.95	230.96	3.70	81.40	2.08	9.70	0.09	0.0	3.7	0.02	2.62	5293824	52
HD 60737	910.07	6.55	569.23	6.95	202.08	1.51	24.10	0.22	17.7	11.1	0.02	2.62	5267712	52
HD 61005	753.53	5.42	472.32	5.76	169.19	1.12	41.49	0.37	628.7	11.1	0.02	2.62	5266944	52
HD 61994	2103.13	15.14	1291.84	17.11	471.04	3.11	51.98	0.47	6.9	6.9	0.02	2.62	5394176	53
HD 64324	929.20	6.69	585.16	7.14	207.22	1.37	23.76	0.21	6.3	9.9	0.02	2.62	5400320	54
HD 66751	2683.46	19.32	1682.98	20.53	600.21	3.96	66.35	0.60	6.0	7.2	0.02	2.62	5408768	54
HD 69076	791.83	5.70	492.67	6.01	177.87	2.21	20.14	0.18	0.4	8.4	0.02	2.62	5421568	54
HD 70516	995.64	7.17	623.34	7.61	227.16	1.50	25.38	0.23	8.4	6.9	0.02	2.62	5292288	52
HD 70573	381.64	2.75	239.73	2.92	86.39	0.57	10.41	0.09	14.8	5.7	0.10	2.62	5308928	53
HD 71974	1889.06	13.60	1168.70	14.26	423.82	2.80	47.65	0.43	16.4	7.9	0.02	2.62	5393408	53
HD 72687	590.63	4.25	369.65	4.51	133.01	1.44	18.80	0.17	3.2	8.7	0.02	2.62	6600448	65
HD 72905	6226.53	44.83	3915.21	47.77	1411.52	9.32	163.5	1.50	44.5	5.4	0.02	2.62	5362688	40
HD 73668	1401.43	10.09	881.16	10.75	313.64	2.07	35.39	0.32	10.5	10.4	0.02	2.62	5435392	54
HD 75302	1315.76	9.47	819.18	9.99	293.72	1.94	32.70	0.29	1.4	8.6	0.02	2.62	5404160	54
HD 75393	1244.85	8.96	787.10	9.60	281.09	1.85	31.70	0.29	-6.2	9.0	0.02	2.62	5341184	53
HD 76218	1329.90	9.57	833.15	10.16	300.52	1.98	33.66	0.30	-5.1	10.0	0.02	2.62	5373696	53
HD 77407	1910.85	13.76	1211.53	14.78	444.45	2.93	49.20	0.44	11.1	9.3	0.02	2.62	5311232	53
HD 80606	339.01	2.44	210.02	2.56	75.52	0.50	8.65	0.08	3.4	5.2	0.10	2.62	5443840	54
HD 85301	1050.80	7.57	652.06	7.96	234.22	2.30	36.80	0.33	38.5	7.0	0.02	2.62	5399552	54
HD 86356	186.44	1.34	117.14	1.43	42.97	0.28	5.12	0.05	-2.6	4.3	0.10	9.96	5260032	52
HD 88201	1022.26	7.36	644.98	7.87	229.89	1.52	25.62	0.23	-1.2	7.3	0.02	2.62	5347328	53
HD 88742	2966.24	21.36	1865.15	22.75	663.21	4.38	73.26	0.66	8.4	8.9	0.02	2.62	5422336	54

Table 1—Continued

Source	IRAC 3.6μm		IRAC 4.5μm		IRAC 8μm		MIPS 24μm		MIPS 70μm		IRAC	MIPS 24μm	AORKE	
	S_ν (Jy)	$\sigma_{\rm int}$ (Jy)	S_ν (Jy)	$\sigma_{\rm int}$ (Jy)	S_ν (Jy)	$\sigma_{\rm int}$ (Jy)	S_ν (Jy)	$\sigma_{\rm int}$ (Jy)	S_ν (Jy)	$\sigma_{\rm int}$ (Jy)	frame time (sec)	DCE Time (sec)	IRAC	M
HD 90712	1043.36	7.51	666.66	8.13	235.39	1.55	26.13	0.24	-2.7	8.0	0.02	2.62	5337344	53
HD 90905	1788.78	12.88	1126.18	13.74	401.52	2.65	49.73	0.45	22.3	11.4	0.02	2.62	5335808	53
HD 91782	573.48	4.13	361.12	4.41	127.76	1.36	14.78	0.13	-1.9	7.5	0.02	2.62	5331200	53
HD 91962	2018.84	14.54	1264.75	15.43	457.91	3.02	50.77	0.46	-0.4	7.8	0.02	2.62	5341952	53
HD 92788	1447.46	10.42	891.20	10.87	322.72	2.13	36.08	0.32	11.2	9.1	0.02	2.62	5440000	54
HD 92855	1280.32	9.22	810.92	9.89	288.82	1.91	32.43	0.29	9.8	6.8	0.02	2.62	5331968	53
HD 95188	627.15	4.51	391.95	4.78	140.03	0.92	15.95	0.14	6.1	9.5	0.02	2.62	5344256	53
HD 98553	1067.94	7.69	669.07	8.16	238.75	1.58	26.35	0.24	3.9	8.0	0.02	2.62	5408000	54
HD 100167	1361.36	9.80	855.45	10.44	307.60	2.03	34.35	0.31	-2.9	8.7	0.02	2.62	5420032	54
HD 101472	1036.87	7.46	665.02	8.11	233.44	1.77	26.19	0.24	-0.6	8.8	0.02	2.62	5342720	53
HD 101959	1612.53	11.61	1013.24	12.36	361.27	2.38	40.18	0.36	9.8	8.4	0.02	2.62	5418496	54
HD 102071	1103.79	7.95	679.71	8.29	246.67	1.63	27.71	0.25	9.5	7.4	0.02	2.62	5423104	54
HD 103432	676.31	4.87	425.79	5.20	150.78	1.13	16.82	0.15	8.4	9.8	0.02	2.62	5428480	54
HD 104467	535.57	3.86	336.17	4.10	121.77	0.88	14.16	0.13	-1.9	5.0	0.02	2.62	5208320	52
HD 104576	616.98	4.44	383.90	4.68	142.62	1.60	16.22	0.15	6.9	8.0	0.02	2.62	5332736	53
HD 104860	724.76	5.22	455.33	5.55	162.49	1.13	19.89	0.18	183.1	7.4	0.02	2.62	5270016	52
HD 105631	1613.93	11.62	989.25	12.07	360.21	2.38	40.27	0.36	1.0	7.4	0.02	2.62	5415424	54
HD 106156	1012.92	7.29	623.21	7.60	227.72	1.50	25.47	0.23	15.1	9.3	0.02	2.62	5423872	54
HD 106252	1200.09	8.64	746.45	9.11	270.92	1.79	30.58	0.28	16.5	9.4	0.02	2.62	5442304	54
HD 106772	992.21	7.14	630.40	7.69	232.27	1.85	26.40	0.24	-4.6	6.8	0.02	2.62	5301504	53
HD 107146	1711.29	12.32	1074.76	13.11	384.40	2.54	59.76	0.54	669.1	9.6	0.02	2.62	5312000	53
HD 107441	254.97	1.84	161.86	1.98	58.42	0.39	7.24	0.07	1.6	7.2	0.10	2.62	5234432	52
HD 108799	3417.14	24.60	2165.72	26.42	767.08	5.06	85.26	0.77	5.0	10.2	0.02	2.62	5338112	53
HD 108944	1136.76	8.19	727.64	8.88	256.94	1.70	28.88	0.26	1.7	8.4	0.02	2.62	5334272	53
HD 111170	373.25	2.69	234.54	3.14	86.24	0.57	10.27	0.09	-4.9	9.2	0.10	2.62	5213696	52
HD 112196	1734.86	12.49	1098.91	13.41	395.59	2.61	43.62	0.39	3.2	9.1	0.02	2.62	5278464	52
HD 115043	2122.18	15.28	1336.87	16.31	476.04	3.14	53.18	0.48	-0.5	7.8	0.02	2.62	6600960	65
HD 116099	111.96	0.81	70.52	0.86	25.38	0.17	3.53	0.03	3.4	3.3	0.10	9.96	5229056	52
HD 117524	223.38	1.61	139.71	1.70	51.23	0.34	6.12	0.06	-10.1	9.9	0.10	9.96	5231360	52
HD 119269	267.91	1.93	168.94	2.06	61.61	0.41	7.40	0.07	21.6	10.5	0.10	2.62	5239040	52
HD 120812	200.55	1.44	127.58	1.56	46.06	0.30	5.57	0.05	-8.9	7.9	0.10	9.96	5227520	52
HD 121320	928.87	6.69	581.52	7.09	209.87	1.39	23.04	0.21	2.1	9.7	0.02	2.62	5424640	54
HD 121504	1001.83	7.21	630.62	7.69	225.25	1.49	25.01	0.23	27.2	18.7	0.02	2.62	5437696	54
HD 122652	1260.59	9.08	795.28	9.70	283.09	1.87	35.22	0.32	83.1	9.1	0.02	2.62	5427712	54
HD 126670	216.52	1.56	137.21	1.67	49.79	0.33	6.17	0.07	-0.8	5.7	0.10	2.62	5212928	52
HD 128242	224.73	1.62	143.13	1.75	52.02	0.34	6.32	0.06	-6.3	5.8	0.10	9.96	5226752	52
HD 129333	1252.51	9.02	790.35	9.64	285.15	1.88	32.83	0.30	6.3	6.3	0.02	2.62	5265409	52
HD 132173	913.26	6.58	577.37	7.04	205.21	1.35	24.11	0.22	-0.8	9.9	0.02	2.62	5333504	53
HD 133295	1343.76	9.68	852.62	10.40	301.06	1.99	34.10	0.31	12.2	12.4	0.02	2.62	5366784	53
HD 133938	128.42	0.93	81.78	1.00	29.60	0.20	3.48	0.03	-5.0	11.5	0.10	9.96	5280768	52
HD 134319	548.74	3.95	339.31	4.14	121.37	0.80	15.41	0.14	-3.4	8.1	0.02	2.62	5307392	53
HD 135363	1045.48	7.53	660.17	8.05	241.28	2.27	28.18	0.25	0.1	7.1	0.02	2.62	5293056	52
HD 136923	2175.65	15.66	1356.06	16.54	489.09	3.23	54.16	0.49	11.3	7.6	0.02	2.62	5429248	54
HD 138004	1208.71	8.70	749.81	9.15	269.34	1.78	29.76	0.27	1.6	7.3	0.02	2.62	5433088	54

Table 1—Continued

Source	IRAC 3.6μm		IRAC 4.5μm		IRAC 8μm		MIPS 24μm		MIPS 70μm		IRAC	MIPS 24μm	AORKE	
	S_ν (Jy)	$\sigma_{\rm int}$ (Jy)	S_ν (Jy)	$\sigma_{\rm int}$ (Jy)	S_ν (Jy)	$\sigma_{\rm int}$ (Jy)	S_ν (Jy)	$\sigma_{\rm int}$ (Jy)	S_ν (Jy)	$\sigma_{\rm int}$ (Jy)	frame time (sec)	DCE Time (sec)	IRAC	M
HD 139498	287.36	2.07	181.71	2.22	66.48	0.44	7.89	0.10	-7.4	15.7	0.10	2.62	5228288	52
HD 139813	1843.07	13.27	1151.04	14.04	419.79	2.77	46.37	0.42	15.6	7.7	0.02	2.62	5336576	53
HD 140374	224.05	1.61	139.56	1.70	50.59	0.33	5.79	0.05	-12.3	11.7	0.10	9.96	5224448	52
HD 141521	245.93	1.77	153.00	1.87	56.64	0.37	6.70	0.07	-10.6	12.5	0.10	2.62	5225216	52
HD 141937	1392.65	10.03	872.31	10.64	310.76	2.05	34.94	0.31	-2.8	11.6	0.02	2.62	5441536	54
HD 141943	849.12	6.11	541.02	6.60	193.09	1.47	27.34	0.25	37.6	15.0	0.02	2.62	5252608	52
HD 142229	690.86	4.97	438.40	5.35	152.19	1.13	17.70	0.16	2.8	8.5	0.02	2.62	5384960	53
HD 142361	459.81	3.31	292.68	3.57	107.66	0.80	12.74	0.11	12.2	19.4	0.02	2.62	5241344	52
HD 143006	1069.37	7.70	929.86	11.34	792.11	5.23	2130	106.00	3795.1	33.3	0.02	2.62	5197312	51
HD 143358	173.57	1.25	111.01	1.35	40.14	0.28	5.22	0.05	2.1	14.8	0.10	9.96	5236736	52
HD 145229	1128.81	8.13	717.36	8.75	254.00	1.68	31.02	0.28	64.4	7.3	0.02	2.62	5387264	53
HD 146516	203.17	1.46	129.34	1.58	46.83	0.31	5.79	0.05	4.1	11.4	0.10	9.96	5218304	52
HD 150554	820.15	5.91	523.93	6.39	181.49	1.58	20.50	0.18	-6.6	6.9	0.02	2.62	5443072	54
HD 150706	1715.11	12.35	1077.03	13.14	388.12	2.56	44.93	0.40	41.3	8.0	0.02	2.62	5385728	53
HD 151798	746.39	5.37	467.61	5.71	166.72	1.10	18.67	0.17	-5.0	16.9	0.02	2.62	5276160	52
HD 152555	819.35	5.90	515.58	6.29	185.47	1.22	20.59	0.19	-0.5	9.6	0.02	2.62	5330432	53
HD 153458	742.93	5.35	465.17	5.67	165.26	1.15	18.90	0.17	-5.4	11.6	0.02	2.62	5416192	54
HD 154417	3993.62	28.75	2506.84	30.58	897.07	5.92	100.9	0.90	5.2	8.5	0.02	2.62	5398784	53
HD 157664	616.87	4.44	391.44	4.78	136.12	0.90	15.36	0.14	3.1	8.2	0.02	2.62	5445376	54
HD 159222	2730.18	19.66	1715.21	20.93	613.30	4.05	67.39	0.61	5.6	7.2	0.02	2.62	5436160	54
HD 161897	1217.95	8.77	754.95	9.21	273.67	1.81	30.18	0.27	-1.8	11.6	0.02	2.62	5430016	54
HD 167389	1210.09	8.71	762.22	9.30	269.59	1.78	29.97	0.27	-4.4	9.2	0.02	2.62	5433856	54
HD 170778	1076.58	7.75	681.74	8.32	241.21	1.59	27.23	0.25	3.9	6.3	0.02	2.62	5369856	53
HD 172649	929.58	6.69	595.15	7.26	208.44	2.24	23.82	0.21	-1.2	7.7	0.02	2.62	5335040	53
HD 174656	362.01	2.61	227.08	2.77	83.19	0.55	10.25	0.09	1.6	4.5	0.10	2.62	5195776	51
HD 179949	2942.99	21.19	1849.03	22.56	658.41	4.34	73.94	0.67	-4.8	10.6	0.02	2.62	5440768	54
HD 183216	1430.42	10.30	896.03	10.93	320.78	2.12	39.41	0.35	22.8	10.2	0.02	2.62	5401856	54
HD 187897	1495.45	10.77	934.10	11.40	338.68	2.23	39.79	0.36	61.6	8.2	0.02	2.62	5419264	54
HD 190228	2068.09	14.89	1282.73	15.65	469.44	3.10	52.77	0.47	11.7	25.5	0.02	2.62	5438464	54
HD 191089	1071.72	7.72	678.37	8.28	242.17	1.60	185.6	1.70	544.3	12.5	0.02	2.62	5363968	53
HD 193017	1179.47	8.49	743.73	9.07	264.71	1.75	29.90	0.27	6.6	9.3	0.02	2.62	5410048	54
HD 195034	1689.95	12.17	1060.98	12.94	379.42	2.50	41.94	0.38	1.6	8.4	0.02	2.62	5426176	54
HD 199019	745.17	5.37	473.60	5.78	165.29	1.09	18.93	0.17	9.0	7.8	0.02	2.62	5343488	53
HD 199143	1401.22	10.09	899.64	10.98	320.68	2.42	37.60	0.34	9.2	11.1	0.02	2.62	5254144	52
HD 199598	1843.53	13.27	1165.87	14.22	412.16	2.72	46.64	0.42	6.9	7.8	0.02	2.62	5413120	54
HD 200746	814.31	5.86	519.15	6.33	183.35	1.30	20.80	0.19	11.4	8.1	0.02	2.62	5371392	53
HD 201219	816.37	5.88	508.54	6.20	181.28	1.20	21.97	0.20	42.4	7.2	0.02	2.62	5396480	53
HD 201989	1440.45	10.37	902.15	11.01	323.35	2.13	36.16	0.33	-0.2	9.5	0.02	2.62	5394944	53
HD 202108	1440.33	10.37	902.09	11.01	321.78	2.12	35.98	0.32	-0.3	9.6	0.02	2.62	5416960	54
HD 202917	519.16	3.74	320.83	3.91	117.29	1.44	19.20	0.17	37.1	5.9	0.02	2.62	5251328	45
HD 203030	613.14	4.42	382.11	4.66	137.07	0.91	15.56	0.14	6.5	7.4	0.02	2.62	5338880	53
HD 204277	1847.54	13.30	1172.19	14.30	415.82	2.74	48.88	0.44	29.6	10.6	0.02	2.62	5374464	53
HD 205905	2172.60	15.64	1366.13	16.67	491.11	3.24	54.34	0.49	17.1	8.9	0.02	2.62	5404928	54
HD 206374	1389.08	10.00	871.06	10.63	312.08	2.06	35.22	0.32	18.1	6.7	0.02	2.62	5414656	54

Table 1—Continued

Source	IRAC 3.6μm		IRAC 4.5μm		IRAC 8μm		MIPS 24μm		MIPS 70μm		IRAC	MIPS 24μm	AORK	
	S_ν (Jy)	$\sigma_{\rm int}$ (Jy)	S_ν (Jy)	$\sigma_{\rm int}$ (Jy)	S_ν (Jy)	$\sigma_{\rm int}$ (Jy)	S_ν (Jy)	$\sigma_{\rm int}$ (Jy)	S_ν (Jy)	$\sigma_{\rm int}$ (Jy)	frame time (sec)	DCE Time (sec)	IRAC	
HD 209253	2008.37	14.46	1285.28	15.68	454.49	3.00	55.94	0.50	75.0	9.2	0.02	2.62	5364480	5
HD 209393	856.52	6.17	531.63	6.49	192.30	1.84	21.74	0.20	-2.4	9.0	0.02	2.62	5368320	5
HD 209779	1295.17	9.32	812.17	9.91	292.11	2.16	32.90	0.30	9.8	11.6	0.02	2.62	5369088	5
HD 212291	907.89	6.54	570.73	6.96	205.97	1.36	22.72	0.20	8.0	7.6	0.02	2.62	5420800	5
HD 216275	1379.27	9.93	867.30	10.58	309.52	2.04	34.54	0.31	7.3	10.5	0.02	2.62	5434624	5
HD 216803	8665.98	62.40	5318.78	64.89	1969.21	13.00	224.3	2.00	27.5	5.3	0.02	2.62	5255680	4
HD 217343	1252.13	9.02	782.38	9.54	282.44	1.86	32.64	0.29	-0.8	9.2	0.02	2.62	5269248	5
HD 219498	313.21	2.25	196.15	2.39	70.45	0.47	10.53	0.09	22.8	3.7	0.10	2.62	5357312	5
HD 224873	625.86	4.51	388.50	4.74	140.78	0.93	15.50	0.14	-6.7	8.5	0.02	2.62	5346560	5
HD 245567	277.75	2.00	175.57	2.14	64.72	0.43	7.32	0.08	-27.0	17.5	0.10	2.62	5248256	5
HD 279788	118.00	0.85	74.32	0.91	26.84	0.18	3.52	0.03	2.6	11.4	0.10	9.96	5245952	5
HD 281691	133.87	1.10	83.68	1.02	30.45	0.20	4.12	0.04	-1.8	6.1	0.10	9.96	5259264	5
HD 282346	306.09	2.20	190.62	2.33	70.26	0.46	8.19	0.08	-20.3	10.3	0.10	2.62	5303040	5
HD 284135	237.70	1.71	149.74	1.83	53.60	0.35	6.36	0.08	7.8	5.8	0.10	2.62	5206784	5
HD 284266	110.21	0.79	69.84	0.85	24.99	0.17	3.14	0.03	-2.9	12.6	0.10	9.96	5220608	5
HD 285281	280.25	2.02	176.07	2.15	64.82	0.43	7.80	0.08	-1.9	4.6	0.10	2.62	5216000	5
HD 285372	93.54	0.67	58.77	0.72	21.50	0.17	2.55	0.03	-4.5	9.4	0.10	9.96	5209856	5
HD 285751	91.46	0.66	56.25	0.70	20.74	0.17	2.64	0.03	-2.2	11.0	0.10	9.96	5207552	5
HD 285840	102.52	0.74	64.06	0.78	23.50	0.15	2.81	0.03	-3.1	7.4	0.40	9.96	5359616	5
HD 286179	124.11	0.89	77.97	0.95	28.01	0.18	3.28	0.04	-4.6	9.3	0.10	9.96	5221376	5
HD 286264	267.39	1.93	167.19	2.04	62.31	0.41	7.56	0.09	-6.8	8.0	0.10	2.62	5250560	5
HE 350	56.95	0.41	36.36	0.44	13.10	0.09	1.63	0.02	6.0	9.8	0.40	9.96	5283072	5
HE 373	51.15	0.37	32.44	0.40	11.87	0.08	1.42	0.02	-3.0	4.6	0.40	9.96	5283840	5
HE 389	46.64	0.34	29.26	0.36	10.55	0.07	1.22	0.02	-0.1	10.4	0.40	9.96	5284608	5
HE 622	44.63	0.32	28.14	0.34	10.31	0.07	1.21	0.02	1.9	10.7	0.40	9.96	5285376	5
HE 696	39.98	0.29	25.79	0.32	9.12	0.06	1.07	0.02	-20.2	11.0	0.40	9.96	5286144	5
HE 699	51.39	0.37	32.70	0.40	11.95	0.14	1.40	0.02	4.0	5.7	0.40	9.96	5286912	5
HE 750	64.83	0.47	41.00	0.50	14.58	0.10	2.04	0.02	-14.4	10.5	0.40	9.96	5287680	5
HE 767	62.88	0.45	39.80	0.49	14.11	0.09	1.66	0.02	-0.030	6.6	0.40	9.96	5288448	5
HE 848	115.60	0.83	72.57	0.89	25.57	0.23	4.60	0.04	-7.9	11.7	0.10	9.96	5289216	5
HE 935	123.07	0.89	78.43	0.96	28.01	0.18	3.37	0.03	-8.8	9.1	0.10	9.96	5289984	5
HE 1101	56.66	0.41	35.34	0.43	12.88	0.09	1.50	0.02	-9.7	10.3	0.40	9.96	5290752	5
HE 1234	76.28	0.55	47.58	0.58	16.99	0.11	1.96	0.02	-9.7	17.2	0.40	9.96	5291520	5
HII 120	67.09	0.48	42.19	0.52	15.18	0.10	1.80	0.03	-11.4	16.5	0.40	9.96	5327360	5
HII 152	67.45	0.49	42.40	0.52	15.16	0.10	2.42	0.03	12.3	14.1	0.40	9.96	6601984	6
HII 173	86.27	0.62	53.77	0.66	19.61	0.13	2.33	0.03	-5.0	11.0	0.40	9.96	5315072	5
HII 174	54.74	0.39	34.10	0.42	12.48	0.08	1.50	0.03	4.9	11.6	0.40	9.96	5315840	5
HII 250	69.23	0.50	44.33	0.54	15.83	0.10	2.12	0.03	4.3	12.2	0.40	9.96	5316608	5
HII 314	80.46	0.58	50.32	0.61	18.23	0.12	2.24	0.03	3.2	14.3	0.40	9.96	5314304	5
HII 514	70.16	0.51	44.24	0.54	15.99	0.11	2.34	0.03	9.8	9.3	0.40	9.96	5317376	5
HII 1015	74.81	0.54	47.49	0.58	16.95	0.11	2.02	0.03	-24.6	11.4	0.40	9.96	5318912	5
HII 1101	91.63	0.66	58.04	0.71	20.89	0.14	3.78	0.03	18.0	14.1	0.40	9.96	6601728	6
HII 1182	77.97	0.56	48.91	0.60	17.49	0.12	2.10	0.03	-4.1	5.4	0.40	9.96	5319680	5
HII 1200	112.26	0.81	71.86	0.88	25.02	0.17	3.43	0.03	-22.2	15.6	0.10	9.96	5325824	5

Table 1—Continued

Source	IRAC 3.6μm		IRAC 4.5μm		IRAC 8μm		MIPS 24μm		MIPS 70μm		IRAC	MIPS 24μm	A
	S_ν (Jy)	$\sigma_{\rm int}$ (Jy)	S_ν (Jy)	$\sigma_{\rm int}$ (Jy)	S_ν (Jy)	$\sigma_{\rm int}$ (Jy)	S_ν (Jy)	$\sigma_{\rm int}$ (Jy)	S_ν (Jy)	$\sigma_{\rm int}$ (Jy)	frame time (sec)	DCE Time (sec)	IRA(
HII 1776	62.92	0.45	39.69	0.48	14.42	0.10	1.75	0.03	-6.1	11.1	0.40	9.96	53281
HII 2147	108.24	0.78	67.89	0.83	24.55	0.17	2.98	0.03	-4.5	5.7	0.10	9.96	53053
HII 2278	91.16	0.66	56.95	0.69	20.87	0.14	2.49	0.03	-14.9	9.9	0.40	9.96	53212
HII 2506	85.60	0.62	54.11	0.66	19.23	0.13	2.33	0.03	5.7	4.6	0.40	9.96	53219
HII 2644	54.39	0.39	33.97	0.41	12.22	0.08	1.43	0.03	3.8	6.6	0.40	9.96	53288
HII 2786	83.50	0.64	53.36	0.65	18.84	0.12	2.20	0.03	2.0	9.8	0.40	9.96	53227
HII 2881	68.28	0.49	43.24	0.53	15.74	0.10	1.78	0.03	8.1	5.9	0.40	9.96	53235
HII 3097	67.41	0.48	42.31	0.52	15.13	0.10	1.84	0.03	-5.7	4.9	0.40	9.96	53242
HII 3179	101.55	0.73	64.27	0.78	22.48	0.15	2.70	0.03	-3.7	3.9	0.10	9.96	53250
HIP 6276	676.70	4.87	418.39	5.10	154.80	1.79	19.26	0.17	13.7	10.6	0.02	2.62	53457
HIP 42491	705.78	5.08	431.44	5.26	157.50	1.53	17.63	0.16	-8.1	11.9	0.02	2.62	54095
HIP 59154	484.75	3.49	294.26	3.59	110.98	0.99	12.92	0.12	0.9	6.0	0.02	2.62	53603
HIP 76477	154.54	1.11	96.58	1.18	35.86	0.24	4.35	0.04	-0.9	8.8	0.10	9.96	52106
MML 1	228.93	1.65	142.01	1.73	52.77	0.35	6.64	0.07	3.3	6.1	0.10	2.62	52405
MML 8	167.52	1.21	104.59	1.28	38.44	0.25	7.81	0.07	17.8	12.9	0.10	9.96	52382
MML 9	165.99	1.20	103.17	1.26	37.89	0.25	4.79	0.04	-6.2	6.7	0.10	9.96	52375
MML 17	228.11	1.64	145.00	1.77	52.24	0.34	9.85	0.09	18.0	7.6	0.10	2.62	52321
MML 18	147.31	1.06	91.80	1.12	33.81	0.22	3.95	0.04	-7.4	11.4	0.10	9.96	52776
MML 26	138.07	0.99	86.42	1.05	31.47	0.24	3.72	0.03	-1.6	8.1	0.10	9.96	52305
MML 28	92.92	0.67	57.95	0.71	21.45	0.14	3.55	0.03	10.1	10.1	0.40	9.96	52769
MML 32	132.67	0.95	84.46	1.03	30.41	0.20	3.72	0.03	6.4	12.0	0.10	9.96	52359
MML 36	216.06	1.56	135.16	1.79	49.64	0.33	8.95	0.08	3.9	4.1	0.10	9.96	52352
MML 38	108.23	0.78	68.47	0.83	24.83	0.16	3.12	0.03	-1.0	5.9	0.10	9.96	52336
MML 40	124.46	0.90	78.01	0.95	28.80	0.19	3.48	0.03	-3.2	4.5	0.10	9.96	52398
MML 43	116.39	0.84	73.09	0.89	26.79	0.18	3.62	0.03	-7.6	8.0	0.10	9.96	52328
MML 51	146.14	1.05	92.99	1.14	34.52	0.23	4.17	0.04	2.0	3.7	0.10	9.96	52121
MML 57	118.05	0.85	74.25	0.91	26.93	0.18	3.55	0.03	7.7	12.7	0.10	9.96	52298
PDS 66	656.79	4.73	521.43	6.36	470.62	3.11	1874	94.00	1672.0	14.9	0.02	2.62	51980
QT And	324.14	2.33	204.36	2.49	76.23	0.50	9.12	0.08	-8.4	5.8	0.10	2.62	52992
R3	58.19	0.42	36.27	0.59	13.34	0.09	1.52	0.02	-10.5	9.0	0.40	9.96	52723
R45	63.91	0.46	40.38	0.49	14.43	0.10	1.90	0.02	2.3	21.4	0.40	9.96	52738
R83	68.66	0.49	43.22	0.53	15.61	0.10	1.80	0.02	-24.7	12.8	0.40	9.96	52730
REJ0137 + 18A	662.72	9.43	413.67	5.05	151.77	1.00	17.50	0.16	2.7	4.5	0.02	2.62	52421
REJ0723 + 20	545.19	3.92	338.81	4.13	125.47	0.83	15.26	0.14	1.0	5.0	0.02	2.62	53480
RXJ0258.4 + 2947	71.67	0.52	44.92	0.55	16.40	0.11	1.92	0.02	-5.3	4.0	0.40	9.96	53580
RXJ0329.1 + 0118	63.93	0.46	40.80	0.50	14.68	0.10	1.71	0.02	2.1	4.8	0.40	9.96	53527
RXJ0331.1 + 0713	179.78	1.29	112.98	1.38	42.16	0.28	4.94	0.04	-4.7	5.3	0.10	9.96	52428
RXJ0354.4 + 0535	103.00	0.74	65.35	0.80	23.61	0.18	3.09	0.03	-7.2	5.0	0.10	9.96	52999
RXJ0357.3 + 1258	77.05	0.56	48.40	0.59	17.72	0.12	2.20	0.03	-3.3	5.7	0.40	9.96	52561
RXJ0434.3 + 0226	48.51	0.35	31.07	0.38	11.46	0.08	1.38	0.02	-5.9	4.1	0.40	9.96	53007
RXJ0442.5 + 0906	67.02	0.48	41.52	0.51	15.23	0.10	1.75	0.03	1.2	4.5	0.40	9.96	53045
RXJ0849.2 − 7735	1444.48	10.40	881.70	10.76	336.69	2.22	39.20	0.35	3.1	8.0	0.02	2.62	53127
RXJ0850.1 − 7554	98.81	0.71	61.45	0.75	22.27	0.15	2.78	0.03	3.3	3.5	0.10	9.96	52984
RXJ0853.1 − 8244	72.44	0.52	45.83	0.56	17.03	0.11	2.05	0.02	-5.3	3.3	0.40	9.96	53511

Table 1—Continued

Source	IRAC 3.6μm		IRAC 4.5μm		IRAC 8μm		MIPS 24μm		MIPS 70μm		IRAC frame time (sec)	MIPS 24μm DCE Time (sec)
	S_ν (Jy)	$\sigma_{\rm int}$ (Jy)	S_ν (Jy)	$\sigma_{\rm int}$ (Jy)	S_ν (Jy)	$\sigma_{\rm int}$ (Jy)	S_ν (Jy)	$\sigma_{\rm int}$ (Jy)	S_ν (Jy)	$\sigma_{\rm int}$ (Jy)		
RXJ0917.2 − 7744	91.21	0.66	57.60	0.70	20.83	0.14	2.38	0.02	3.1	3.3	0.40	9.96
RXJ1111.7 − 7620	447.93	3.23	363.46	4.43	198.69	1.86	229.6	2.10	224.3	8.3	0.02	2.62
RXJ1140.3 − 8321	114.19	0.82	69.97	0.85	26.43	0.17	3.02	0.03	-2.0	5.0	0.10	9.96
RXJ1203.7 − 8129	71.75	0.52	45.29	0.55	16.61	0.11	1.99	0.02	2.6	4.7	0.40	9.96
RXJ1209.8 − 7344	163.91	1.18	102.40	1.25	38.64	0.26	4.62	0.04	-4.4	5.0	0.10	9.96
RXJ1220.6 − 7539	200.62	1.45	124.54	1.52	46.07	0.30	5.48	0.05	-12.4	4.3	0.10	9.96
RXJ1225.3 − 7857	112.89	0.81	70.60	0.86	25.73	0.17	3.05	0.03	-0.9	3.9	0.10	9.96
RXJ1450.4 − 3507	178.29	1.28	112.17	1.37	41.31	0.27	4.91	0.04	-3.7	4.0	0.10	9.96
RXJ1457.3 − 3613	149.56	1.08	94.73	1.16	34.38	0.23	4.32	0.04	-1.2	5.4	0.10	9.96
RXJ1458.6 − 3541	211.96	1.53	133.68	1.63	49.73	0.33	5.97	0.05	7.6	4.2	0.10	9.96
RXJ1500.8 − 4331	96.40	0.69	61.33	0.75	22.54	0.15	2.65	0.02	-10.0	8.2	0.40	9.96
RXJ1507.2 − 3505	137.35	0.99	85.39	1.04	31.64	0.21	4.05	0.04	-0.088	6.1	0.10	9.96
RXJ1518.4 − 3738	121.24	0.87	77.05	0.94	28.29	0.19	3.48	0.04	-1.8	5.8	0.10	9.96
RXJ1531.3 − 3329	95.38	0.69	59.77	0.73	21.97	0.14	2.49	0.04	12.4	13.1	0.40	9.96
RXJ1541.1 − 2656	82.17	0.59	51.08	0.62	19.05	0.13	2.27	0.03	-37.2	13.3	0.40	9.96
RXJ1544.0 − 3311	138.34	1.00	87.01	1.06	32.21	0.21	4.04	0.04	-22.4	12.0	0.10	9.96
RXJ1545.9 − 4222	209.09	1.50	131.65	1.61	49.24	0.33	5.83	0.07	-27.9	12.6	0.10	2.62
RXJ1600.6 − 2159	134.55	0.97	85.17	1.04	31.42	0.21	4.38	0.04	9.9	15.7	0.10	9.96
RXJ1839.0 − 3726	112.27	0.81	70.86	0.86	25.95	0.17	3.39	0.04	-7.6	7.2	0.10	9.96
RXJ1841.8 − 3525	187.75	1.35	119.45	1.46	43.02	0.28	5.37	0.05	-1.7	5.3	0.10	9.96
RXJ1842.9 − 3532	269.53	1.94	216.15	2.64	157.35	1.04	358.9	3.20	942.6	13.8	0.10	2.62
RXJ1844.3 − 3541	141.52	1.02	88.66	1.08	32.65	0.22	3.84	0.04	-17.9	6.5	0.10	9.96
RXJ1852.3 − 3700	88.58	0.64	58.49	2.04	33.64	0.97	472.2	4.20	1367.0	14.6	0.02	2.62
RXJ1917.4 − 3756	318.64	2.29	198.72	2.42	73.67	0.49	8.82	0.08	2.1	6.9	0.10	2.62
RXJ2313.0 + 2345	107.93	0.78	67.33	0.82	24.13	0.23	2.80	0.03	-3.3	4.4	0.10	9.96
SAO 150676	306.12	2.20	191.84	2.34	70.27	0.46	8.72	0.08	2.1	4.3	0.10	2.62
SAO 178272	327.04	2.35	203.57	2.48	75.43	0.50	9.08	0.08	1.5	3.5	0.10	2.62
ScoPMS 21	120.69	0.87	76.08	0.93	28.71	0.19	3.62	0.06	-8.1	26.1	0.10	9.96
ScoPMS 27	186.26	1.34	116.92	1.43	43.94	0.29	5.25	0.08	7.3	11.4	0.10	2.62
ScoPMS 52	319.90	2.30	200.77	2.45	75.93	0.50	8.89	0.11	34.5	23.8	0.10	2.62
ScoPMS 214	242.00	1.74	154.41	1.88	59.07	0.39	7.75	0.14	15.1	15.4	0.60	2.62
V343 Nor	1344.03	9.68	846.43	10.33	308.70	2.04	36.77	0.33	-1.3	40.0	0.02	2.62
V383 Lac	752.12	5.42	466.84	5.70	170.11	1.33	20.27	0.18	7.8	8.6	0.02	2.62
W79	42.02	0.30	26.01	0.32	9.52	0.06	1.38	0.02	0.2	13.7	0.40	9.96
[PZ99]J155847.8 − 175800	147.12	1.06	93.15	1.14	35.28	0.23	6.11	0.06	-21.8	14.8	0.40	9.96
[PZ99]J160814.7 − 190833	135.31	0.97	84.71	1.03	31.66	0.23	3.74	0.04	6.4	13.2	0.10	9.96
[PZ99]J161318.6 − 221248	325.68	2.35	204.71	2.50	76.83	0.51	9.14	0.09	-20.8	12.1	0.10	2.62
[PZ99]J161329.3 − 231106	139.25	1.00	87.83	1.07	33.38	0.23	4.12	0.04	12.7	11.1	0.10	9.96
[PZ99]J161402.1 − 230101	119.64	0.86	75.34	0.92	28.25	0.19	3.66	0.04	-19.6	13.0	0.10	9.96
[PZ99]J161411.0 − 230536	498.31	3.59	401.87	4.90	363.52	2.40	304.0	2.70	91.1	11.7	0.02	2.62
[PZ99]J161459.2 − 275023	101.69	0.73	63.27	0.77	23.80	0.16	4.53	0.04	26.6	25.0	0.10	9.96
[PZ99]J161618.0 − 233947	170.49	1.23	106.52	1.30	40.09	0.27	5.35	0.05	-14.8	14.0	0.10	9.96
vB 1	1157.67	8.34	733.56	8.95	259.47	1.71	28.51	0.26	14.1	12.2	0.02	2.62
vB 39	907.63	6.54	581.32	7.09	214.07	1.95	24.26	0.22	-3.5	10.3	0.60	2.62

Table 1—Continued

Source	IRAC 3.6μm		IRAC 4.5μm		IRAC 8μm		MIPS 24μm		MIPS 70μm		IRAC	MIPS 24μm	AORKEY	
	S_ν (Jy)	$\sigma_{\rm int}$ (Jy)	S_ν (Jy)	$\sigma_{\rm int}$ (Jy)	S_ν (Jy)	$\sigma_{\rm int}$ (Jy)	S_ν (Jy)	$\sigma_{\rm int}$ (Jy)	S_ν (Jy)	$\sigma_{\rm int}$ (Jy)	frame time (sec)	DCE Time (sec)	IRAC	MIPS
vB 49	531.47	3.83	333.05	5.62	123.24	1.12	13.61	0.12	-5.8	7.7	0.60	2.62	4096512	5376768
vB 52	856.95	6.17	545.70	6.66	200.27	1.32	22.48	0.20	0.6	10.6	0.60	2.62	4096512	5377280
vB 63	750.87	6.02	480.71	5.87	177.66	1.52	19.97	0.18	3.0	10.7	0.60	2.62	4096512	5377792
vB 64	658.77	4.78	422.85	5.16	152.25	1.00	16.96	0.15	-4.3	11.8	0.60	2.62	4096512	5378304
vB 66	961.97	6.93	609.26	7.43	216.22	1.43	24.58	0.22	10.2	11.4	0.02	2.62	5367552	5368064
vB 73	756.94	5.45	476.39	5.81	176.50	1.17	20.16	0.18	-8.4	10.4	0.60	2.62	4096512	5378816
vB 79	422.74	3.14	266.31	4.12	99.03	1.03	10.95	0.10	-7.6	7.9	0.60	2.62	4096512	5379328
vB 88	741.40	5.34	469.92	5.73	165.43	1.09	18.93	0.17	-11.3	12.5	0.02	2.62	5397248	5397760
vB 91	574.70	4.14	349.43	4.26	131.46	0.87	14.81	0.13	-9.3	12.7	0.60	2.62	4096768	5379840
vB 92	473.38	6.60	291.35	4.07	109.07	0.94	12.07	0.11	-2.6	13.8	0.60	2.62	4096768	5380352
vB 93	330.46	2.38	204.75	2.50	76.29	0.50	8.42	0.08	7.5	8.4	0.60	2.62	4096768	5380864
vB 96	722.91	7.20	449.19	5.48	167.82	1.11	18.54	0.17	-13.6	12.3	0.60	2.62	4096768	5381376
vB 97	730.07	10.70	462.11	5.64	169.52	1.12	19.07	0.17	-5.3	12.0	0.60	2.62	4096768	5381888
vB 99	314.03	2.26	197.40	2.41	73.14	0.48	8.19	0.08	-4.7	12.1	0.60	2.62	4096768	5382400
vB 106	770.31	5.55	479.30	5.85	171.24	1.13	19.42	0.17	10.3	11.5	0.02	2.62	5392640	5393152
vB 142	572.80	4.12	354.86	4.33	128.34	2.14	14.38	0.13	2.2	11.9	0.02	2.62	5329664	5330176
vB 143	626.50	4.51	391.13	4.77	139.51	0.92	15.68	0.14	-4.8	11.3	0.02	2.62	5406464	5406976
vB 176	550.88	7.35	337.21	4.11	128.40	0.95	14.26	0.13	-0.6	7.2	0.60	2.62	4096512	5382912
vB 180	404.68	2.91	251.91	3.07	94.00	1.25	10.52	0.09	2.4	7.1	0.60	2.62	4096768	5383424
vB 183	266.16	1.92	168.22	2.05	63.01	0.43	7.04	0.08	-11.7	12.4	0.60	2.62	4096768	5383936

[1]IRAC photometry performed using aperture radius of 4 pixels

[2]Neighboring source subtracted from MIPS 70um image before measuring photometry

[3]IRAC photometry measured using non-FEPS, archival data

[4]MIPS photometry measured using non-FEPS, archival data

Table 2. Adopted Instrinsic Colors

SpT	$(B-V)_{\rm T}$			$V_{\rm T}-K_s$			$J-K_s$		
	Average	Dispersion	N	Average	Dispersion	N	Average	Dispersion	N
F2	0.383	0.028	74	0.224	0.029	153	0.980	0.093	58
F3	0.433	0.025	147	0.237	0.019	257	1.090	0.057	102
F5	0.483	0.022	266	0.267	0.026	491	1.216	0.069	230
F6	0.527	0.022	214	0.288	0.020	337	1.305	0.058	173
F7	0.558	0.026	250	0.303	0.025	371	1.354	0.050	177
F8	0.592	0.023	130	0.320	0.025	211	1.393	0.043	90
G0	0.632	0.025	206	0.329	0.021	313	1.460	0.041	145
G1	0.648	0.023	114	0.342	0.025	197	1.498	0.067	117
G2	0.669	0.025	167	0.350	0.024	248	1.554	0.069	166
G3	0.707	0.033	324	0.371	0.029	521	1.601	0.047	241
G5	0.754	0.029	331	0.387	0.026	503	1.682	0.064	325
G6	0.801	0.036	175	0.417	0.025	211	1.759	0.059	144
G8	0.852	0.039	186	0.445	0.035	246	1.866	0.088	191
K0	0.936	0.040	183	0.490	0.043	224	2.032	0.124	196
K1	1.001	0.036	102	0.528	0.034	117	2.176	0.095	100
K2	1.064	0.051	95	0.574	0.035	96	2.334	0.114	91
K3	1.150	0.073	98	0.605	0.041	91	2.483	0.126	83
K4	1.272	0.061	43	0.703	0.054	51	2.800	0.160	42
K5	1.420	0.093	22	0.781	0.043	21	3.237	0.222	21